

# UNCLASSIFIED

AD NUMBER
ADB244697
NEW LIMITATION CHANGE
TO Approved for public release, distribution unlimited
FROM Distribution authorized to U.S. Gov't. agencies only; Proprietary Info.; Aug 98. Other requests shall be referred to U.S. Army Medical Research and Materiel Comd., Fort Detrick, MD 21702-5012.
AUTHORITY
USAMRMC ltr, 26 Nov 2002

THIS PAGE IS UNCLASSIFIED

AD \_\_\_\_\_

AWARD NUMBER DAMD17-97-1-7261

TITLE: Non-Invasive Determination of Breast Cancer Oxygen Tension by F-19 NMR and Breast Cancer Physiology in Response to Radiotherapy

PRINCIPAL INVESTIGATOR: Yulin Song

CONTRACTING ORGANIZATION: University of Texas  
Southwestern Medical Center  
Dallas, Texas 75235-9106

REPORT DATE: August 1998

TYPE OF REPORT: Annual

PREPARED FOR: Commander  
U.S. Army Medical Research and Materiel Command  
Fort Detrick, Maryland 21702-5012

DISTRIBUTION STATEMENT: Distribution authorized to U.S. Government agencies only (proprietary information, Aug 98). Other requests for this document shall be referred to U.S. Army Medical Research and Materiel Command, 504 Scott Street, Fort Detrick, Maryland 21702-5012.

The views, opinions and/or findings contained in this report are those of the author(s) and should not be construed as an official Department of the Army position, policy or decision unless so designated by other documentation.

DTIC QUALITY INSPECTED 4

## NOTICE

USING GOVERNMENT DRAWINGS, SPECIFICATIONS, OR OTHER DATA INCLUDED IN THIS DOCUMENT FOR ANY PURPOSE OTHER THAN GOVERNMENT PROCUREMENT DOES NOT IN ANY WAY OBLIGATE THE U.S. GOVERNMENT. THE FACT THAT THE GOVERNMENT FORMULATED OR SUPPLIED THE DRAWINGS, SPECIFICATIONS, OR OTHER DATA DOES NOT LICENSE THE HOLDER OR ANY OTHER PERSON OR CORPORATION; OR CONVEY ANY RIGHTS OR PERMISSION TO MANUFACTURE, USE, OR SELL ANY PATENTED INVENTION THAT MAY RELATE TO THEM.

### LIMITED RIGHTS LEGEND

Contract Number: DAMD17-97-1-7261

Contractor: University of Texas Southwestern Medical Center

Location of Limited Rights Data (Pages): 1-50

Those portions of the technical data contained in this report marked as limited rights data shall not, without the written permission of the above contractor, be (a) released or disclosed outside the government, (b) used by the Government for manufacture or, in the case of computer software documentation, for preparing the same or similar computer software, or (c) used by a party other than the Government, except that the Government may release or disclose technical data to persons outside the Government, or permit the use of technical data by such persons, if (i) such release, disclosure, or use is necessary for emergency repair or overhaul or (ii) is a release or disclosure of technical data (other than detailed manufacturing or process data) to, or use of such data by, a foreign government that is in the interest of the Government and is required for evaluational or informational purposes, provided in either case that such release, disclosure or use is made subject to a prohibition that the person to whom the data is released or disclosed may not further use, release or disclose such data, and the contractor or subcontractor or subcontractor asserting the restriction is notified of such release, disclosure or use. This legend, together with the indications of the portions of this data which are subject to such limitations, shall be included on any reproduction hereof which includes any part of the portions subject to such limitations.

THIS TECHNICAL REPORT HAS BEEN REVIEWED AND IS APPROVED FOR PUBLICATION.

Patricia C. Morrow

5/28/99

# REPORT DOCUMENTATION PAGE

Form Approved  
OMB No. 0704-0188

Public reporting burden for this collection of information is estimated to average 1 hour per response, including the time for reviewing instructions, searching existing data sources, gathering and maintaining the data needed, and completing and reviewing the collection of information. Send comments regarding this burden estimate or any other aspect of this collection of information, including suggestions for reducing this burden, to Washington Headquarters Services, Directorate for Information Operations and Reports, 1215 Jefferson Davis Highway, Suite 1204, Arlington, VA 22202-4302, and to the Office of Management and Budget, Paperwork Reduction Project (0704-0188), Washington, DC 20503.

1. AGENCY USE ONLY (Leave blank)		2. REPORT DATE August 1998	3. REPORT TYPE AND DATES COVERED Annual (1 Aug 97 - 31 Jul 98)	
4. TITLE AND SUBTITLE  Non-Invasive Determination of Breast Cancer Oxygen Tension by F-19 NMR and Breast Cancer Physiology in Response to Radiotherapy			5. FUNDING NUMBERS  DAMD17-97-1-7261	
6. AUTHOR(S)  Yulin Song				
7. PERFORMING ORGANIZATION NAME(S) AND ADDRESS(ES)  University of Texas Southwestern Medical Center Dallas, Texas 75235-9106			8. PERFORMING ORGANIZATION REPORT NUMBER	
9. SPONSORING / MONITORING AGENCY NAME(S) AND ADDRESS(ES)  U.S. Army Medical Research and Materiel Command Fort Detrick, Maryland 21702-5012			10. SPONSORING / MONITORING AGENCY REPORT NUMBER	
11. SUPPLEMENTARY NOTES				
12a. DISTRIBUTION / AVAILABILITY STATEMENT  Distribution authorized to U.S. Government agencies only (proprietary information, Aug 98). Other requests for this document shall be referred to U.S. Army Medical Research and Materiel Command, 504 Scott Street, Fort Detrick, Maryland 21702-5012.			12b. DISTRIBUTION CODE	
13. ABSTRACT (Maximum 200 words)  It has been shown that the efficacy of radiotherapy, chemotherapy and photodynamic therapy are influenced by tumor oxygenation, and hypoxic tumors are refractory. Many techniques for monitoring pO <sub>2</sub> have been developed. Most, however, are invasive. 19F MRI of hexafluorobenzene (HFB), based on PBSR-EPI, provides an alternative non-invasive technique to monitor pO <sub>2</sub> . Implementation of this techniques, however, requires a high quality double-tuned (1H-19F) whole body resonator in order to minize preparation time and prevent accidental death of rat.  Two resonators, one being a double-tuned whole body birdcage resonator and another one slotted tube resonator, have been constructed and tested. Laboratory bench testing and phantom imaging indicated that the birdcage resonator's B1 fields are somewhat heterogenous across usable volume of the resonator for both modes and the slotted tube resonator has high Q values and short 90 degree pulse width, which results in improved sensitivity. The B1 field was found to excellent for 1H resonance and resonably good for 19F resonance.				
14. SUBJECT TERMS Breast Cancer			15. NUMBER OF PAGES 51	
			16. PRICE	
17. SECURITY CLASSIFICATION OF REPORT Unclassified	18. SECURITY CLASSIFICATION OF THIS PAGE Unclassified	19. SECURITY CLASSIFICATION OF ABSTRACT Unclassified	20. LIMITATION OF ABSTRACT Limited	

19990614 078

## FOREWORD

Opinions, interpretations, conclusions and recommendations are those of the author and are not necessarily endorsed by the U.S. Army.

\_\_\_\_ Where copyrighted material is quoted, permission has been obtained to use such material.

\_\_\_\_ Where material from documents designated for limited distribution is quoted, permission has been obtained to use the material.

YS Citations of commercial organizations and trade names in this report do not constitute an official Department of Army endorsement or approval of the products or services of these organizations.

YS In conducting research using animals, the investigator(s) adhered to the "Guide for the Care and Use of Laboratory Animals," prepared by the Committee on Care and use of Laboratory Animals of the Institute of Laboratory Resources, national Research Council (NIH Publication No. 86-23, Revised 1985).

\_\_\_\_ For the protection of human subjects, the investigator(s) adhered to policies of applicable Federal Law 45 CFR 46.

\_\_\_\_ In conducting research utilizing recombinant DNA technology, the investigator(s) adhered to current guidelines promulgated by the National Institutes of Health.

\_\_\_\_ In the conduct of research utilizing recombinant DNA, the investigator(s) adhered to the NIH Guidelines for Research Involving Recombinant DNA Molecules.

\_\_\_\_ In the conduct of research involving hazardous organisms, the investigator(s) adhered to the CDC-NIH Guide for Biosafety in Microbiological and Biomedical Laboratories.

Song Yulin August 27, 98  
PI - Signature Date

# TABLE OF CONTENTS

1. Introduction .....	5
2. Radiofrequency Resonator Design and Testing .....	6
2.1 Functions and Characteristics of RF Resonators .....	6
2.2 Double-Tuned ( $^1\text{H}$ - $^{19}\text{F}$ ) Birdcage Whole Body Resonator .....	7
2.2.1 Design Theory .....	7
2.2.2 Computer Simulation .....	8
2.2.3 Construction .....	11
2.2.4 Bench Testing .....	13
2.2.5 Phantom Imaging .....	15
2.2.6 Discussion .....	20
2.3 Slotted Tube Resonator .....	21
2.3.1 Design Theory .....	21
2.3.2 Construction .....	23
2.3.3 Bench Testing .....	24
2.3.4 Phantom Imaging .....	25
2.3.5 Discussion .....	33
3. Software Development .....	34
3.1 Program to Assess the Goodness of T1 Relaxation Curve Fit .....	34
3.2 Program to Compute HFB Clearance Rate Map .....	35
4. Conclusions .....	36
5. References .....	37
6. Appendix .....	38
6.1 Source Code to Compute HFB Clearance Rate Map .....	38

# 1. Introduction

It has been shown that the efficacy of radiotherapy, chemotherapy and photodynamic therapy are influenced by tumor oxygenation, and hypoxic tumors are refractory. Thus, a reliable non-invasive method of measuring tumor oxygen tension would be valuable in treatment planning. Many techniques for monitoring  $pO_2$  have been developed. Most, however, are invasive (e.g., electrodes, biopsy and cryospectrophotometry) or limited to surface tissues (fluorescence and phosphorescence).  $^{19}F$  MRI of hexafluorobenzene (HFB), based on Pulse Burst Saturation Recovery (PBSR) - Echo Planar Imaging (EPI), provides an alternative non-invasive technique to monitor  $pO_2$  or determine the extent of hypoxia. Implementation of this technique, however, requires a high quality double-tuned ( $^1H$  and  $^{19}F$ ) whole body birdcage resonator or a continuously swithable whole body resonator in order to minimize preparation time and prevent accidental death of rat. The desired imaging and spectroscopy resonator for our purposes would be the one that provides the highest possible signal-to-noise ratio (SNR), a good filling factor, and a highly homogeneous  $B_1$  field. To address these issues, I designed, built, and tested two RF resonators, one being a double-tuned whole body birdcage resonator and another one a swithable whole body slotted tube resonator.

For the birdcage resonator, laboratory bench testing indicated that the unloaded  $Q$ s for both proton and fluorine resonant modes are similar and relatively low. The loaded  $Q$  drops by about 36% for fluorine and 39% for proton. Phantom imaging found that the  $B_1$  fields are somewhat heterogeneous across usable volume of the resonator for both resonant modes. For the slotted tube resonator, laboratory bench testing shown that the resonator has the capability of being continuously tuned in the frequency range of 150 MHz ~ 220 MHz. The resonator has high  $Q$  values and short  $90^\circ$  pulse widths for both proton and fluorine, which results in improved sensitivity and makes *in vivo* tumor  $pO_2$  studies possible. In addition, the  $B_1$  field homogeneity was found to be excellent for proton resonance and reasonably good for fluorine resonance across usable volume of the resonator.

HFB has been found to clear relatively rapidly. Clearance rate may provide an indication of tumor perfusion. To compute the clearance rate on a voxel by voxel basis and thus produce a clearance map, I wrote a Unix based NMR-shell script program. In addition, I wrote another NMR-shell script program to display the T1 relaxation curve and assess the goodness of the curve fit of individual voxels of PBSR-EPI images. The graphical representation of the data, clearance model, relaxation model, and goodness of fit provided a quick and convenient way of assessing the quality of the data. Both programs have been tested.

## 2. RF Resonator Design and Testing

### 2.1 Functions and Characteristics of RF Resonators

The fundamental functions of an NMR radiofrequency (RF) resonator or coil are two fold: (1) to excite the nuclear spins of interest by transmitting a magnetic field  $B_1$  and then after a suitable delay, (2) to receive the resulting signal from the precessing nuclear spin magnetization, called free induction decay (FID). During excitation mode, the RF resonator serves as a transducer that converts RF power into the transverse rotating magnetic field  $B_1$  in the imaging volume of a sample. Therefore, high-transmission efficiency means that the resonator delivers a maximum  $B_1$  to the sample volume with a minimum RF power. During reception mode, the RF resonator, along with its associated preamplifier, acts as a transducer that converts the precessing nuclear spin magnetization into electrical signals suitable for further processing by a computer. High-detection efficiency for the reception mode then corresponds to minimal degradation of the inherent signal-to-noise (SNR) of the sample volume. A well-designed and constructed RF resonator should be highly efficient as a transmitter as well as a receiver.

The NMR signal (FID) is a time-dependent AC voltage induced in the RF resonator by the nuclear spin magnetization vector  $M$  precessing freely in the transverse ( $x'y'$ ) plane. The  $M$  has been nutated into the  $x'y'$  plane by a torque exerted on it by the rotating (pulsed) magnetic field  $B_1$  of appropriate frequency (*Larmor frequency*), time duration, and amplitude. The RF resonator transmits an RF power of the order of hundreds of volts into the sample volume, whereas it receives a voltage from the magnetization  $M$  of the order of one tenth of a microvolt ( $0.1 \mu\text{V}$ ).

The relative orientation of the static magnetic field  $B_0$ , the rotating RF magnetic field  $B_1$  and the precessing magnetization vector  $M$  is crucial in NMR experiments. The  $B_1$  field must be perpendicular to  $B_0$ , and the RF resonator must be oriented in such a way that the precessing magnetization,  $M$ , is perpendicular to the plane of the conductor in order to generate the maximum signal. The main characteristics of a resonator are the frequency,  $\omega$ , at which it resonates, and the quality factor,  $Q$ , which is a measure of the circuit's energy storage efficiency. At resonance, the maximum peak current occurs in the resonator and energy is alternatively stored as magnetic energy in inductor, and then as electrostatic energy in the capacitor. All resonators, regardless of type, must be tuned to the resonant frequency of the nucleus to be studied. They also have to be matched to the input impedance of the preamplifier so that the maximum power is transferred from the resonator to the receiver. Tuning, in general, is performed via a tuning circuit made up of a fixed and variable capacitor, while impedance matching is carried out using a variable capacitor only. The quality



factor  $Q$ , describing the capacity of the resonator to store magnetic energy without resistance losses, is defined as

$$Q = \text{maximum energy stored/average energy dissipated per radian} \quad (1)$$

or

$$Q = \omega/\Delta\omega \quad (2)$$

where  $\Delta\omega$  is defined as the full 3 dB bandwidth. The definition of  $Q$  given by (2) lends itself to laboratory measurements, because measuring both resonant frequency  $\omega$  and bandwidth  $\Delta\omega$  is possible.

A good RF resonator should 1) resonate at the desired operating frequency, 2) have a high  $Q$  factor, 3) have a high signal-to-noise ratio (SNR), 4) have a good filling factor, 5) have a highly homogeneous  $B_1$  field, 6) have minimum resistance losses, 7) be able to withstand the applied voltages, 8) produce minimal electric fields in the sample, 9) have minimum interaction with the rest of the system, 10) permit quadrature excitation and reception, and 11) be large enough to accommodate the imaging sample. This project demanded a new efficient resonator. To address these needs, I designed, built, and tested two RF resonators, one being a double-tuned whole body ( $^1\text{H}$ - $^{19}\text{F}$ ) birdcage resonator and another one a slotted tube resonator.

## 2.2 Double-Tuned ( $^1\text{H}$ - $^{19}\text{F}$ ) Whole Body Birdcage Resonator

This project involved  $^{19}\text{F}$  and  $^1\text{H}$  NMR imaging with living rats in a single experiment, so it was highly desirable to be able to change the resonant frequency without retuning the resonator or disturbing the animal. Thus, I chose to use a highpass birdcage resonator, since it provides not only two or more high resonant frequencies simultaneously, but also the greatest possible signal-to-noise ratio and  $B_1$  field homogeneity [1]. A birdcage resonator consists of a set of  $N$  (2, 4, 8, 16, etc.) copper wires or sheets arranged axially on the surface of a plastic cylinder and connected by high quality RF capacitors at each end. In this configuration, the effective current density in the wires or sheets varies in proportion to  $\cos(\phi)$ , where  $\phi$  is the azimuthal angle in cylindrical coordinates [2], and there exist several possible modes of resonance, two of which have the desired sinusoidal dependence of current on  $\phi$  [3].

### 2.2.1 Design Theory

Assuming perfectly conducting copper sheets, Figure 1 shows part of the simplified circuit model of a birdcage resonator with 16 identical legs (copper sheets), where  $L_i$  is the self inductance of the  $i$ th copper sheet and  $C_i$  is the capacitor connected

between the  $i$ th and the  $(i+1)$ th copper sheet. The self inductance of the short copper sheet used to connect the capacitors at the ends is neglected. This is based on the fact that the electric current in the resonator is longitudinal (along the copper sheet) and maximal at the ends of the resonator.

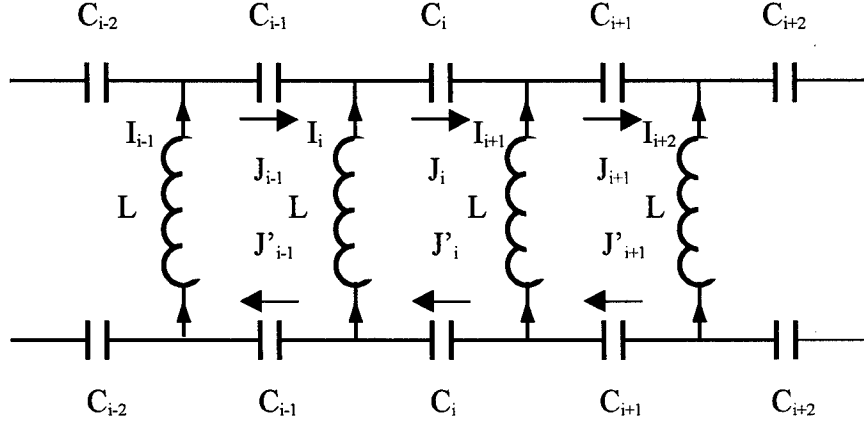


**Figure 1** Part of the equivalent circuit for the high-pass double-tuned whole body birdcage resonator.

By applying Kirchhoff's Law to the  $i$ th loop made up of  $i$ th and  $(i+1)$ th copper sheets and  $i$ th capacitor  $C_i$  and using the complex number notation for AC current and impedance, we can get a linear system of equations:

$$\sum_k i\omega M_{i,k} I_k - \sum_k i\omega M_{i+1,k} I_k - \frac{2i}{\omega C_i} J_i = 0 \quad (1)$$

where  $M_{i,k}$  is the mutual inductance between the  $i$ th and  $k$ th copper sheets,  $J_i$  is the current in the  $i$ th capacitor,  $I_k$  is the current in the  $k$ th copper sheet,  $i$  is the imaginary number, and the summation is carried out over all possible values of index  $k$  from 0 to  $N-1$ .

There are many ways of solving Equation (1), either analytically or numerically. The solution will represent the various resonant modes of operation of the resonator. This circuit model is a simplified one and does not take into account the complications that exist in any real implementation, such as the self-inductance of the capacitors and the inductance of the end rings. Nevertheless, the general form of the model is not altered by these factors, and the qualitative description is still valid.

### 2.2.2 Computer Simulation

Instead of solving the above-described complex equation, I simulated this circuit model on a PC computer using P-Spice [4]. The complete simulation circuit model is shown in Figure 2. The desired resonant frequencies are 188.22 MHz for  $^{19}\text{F}$  and 200.16 MHz for  $^1\text{H}$  in a 4.7 T magnet. The inductance produced by the end rings was neglected in this simulation circuit, since it only accounts for  $\sim 5\%$  of the total inductance. However, the circuit model is adequate for analyzing the essential frequency characteristics of the resonator.

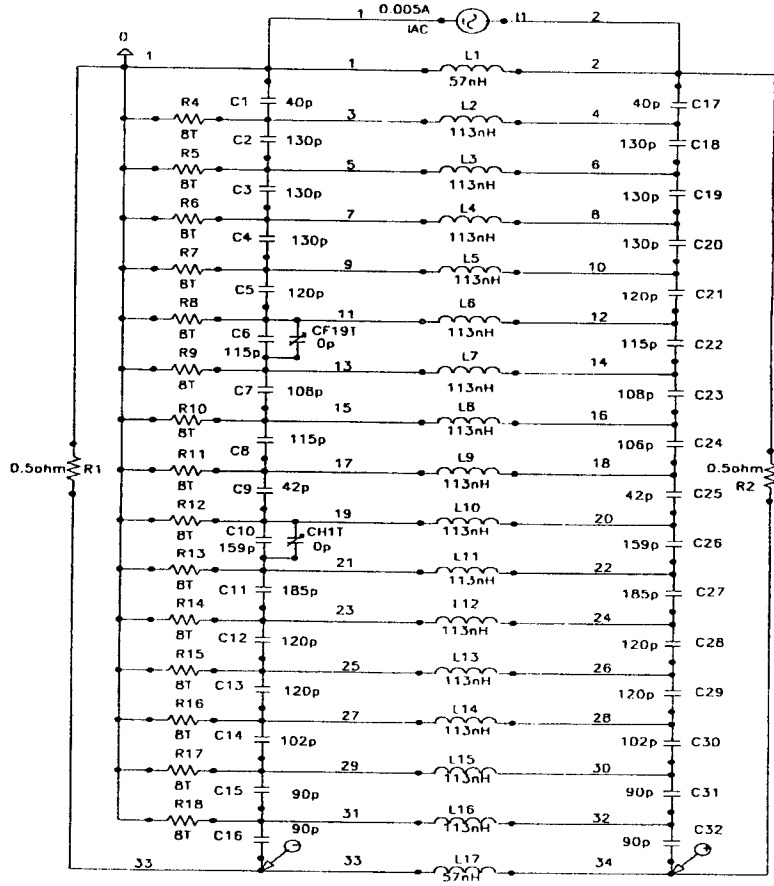


Figure 2 The P-Spice simulation circuit of the double-tuned whole body birdcage resonator.

The first step in simulating this problem was to estimate the inductance of the copper sheets, which is given by [3].

$$L = 2h[ \ln (2h/b) + 1/2 ] \quad (2)$$

where  $L$  is the inductance in nanoHenries,  $h$  is the height in centimeters, and  $b$  is the width in centimeters. The copper sheets have a height of 16.5 cm and a width of 1.0 cm, with a thickness of  $\sim 0.2$  mm. The calculated value of the inductance based on Equation (2) was 113 nH.

The second step was to substitute this value into the simulation circuit, apply an AC current source to the circuit, vary the value of each of the 32 capacitors, and observe the amplitudes of output voltages and resonant frequencies of the circuit until two sharp resonant peaks (188.22 MHz for  $^{19}\text{F}$  and 200.16 MHz for  $^1\text{H}$  in a 4.7 T magnet) with the maximum output voltages were achieved.

The capacitance values for the end ring capacitors obtained from the P-Spice simulation study are tabulated in Table 1. Theoretically speaking, all the capacitance values should be equal for a single-tuned resonator and close to each other for a double-tuned resonator in order to generate a homogeneous  $B_1$  field. The circuit model presented here is a simplified one. Therefore, the capacitance values obtained are not quite close to each other. The simulation study indicates that C10, C26, C11, C27, C12, and C28 are relatively insensitive to  $^{19}\text{F}$  resonant frequency, thus, they could be connected to the  $^1\text{H}$  tuning circuit. I chose to place the tuning circuit in parallel to C10 since this placement provides both the best tuning for  $^1\text{H}$  mode and also stabilizes the  $^{19}\text{F}$  mode.

**Table 1** Capacitance values determined by P-Spice simulation study (unit: pF)

C1	C2	C3	C4	C5	C6	C7	C8
40	130	130	130	120	115	108	115
C9	C10	C11	C12	C13	C14	C15	C16
42	159	185	120	120	102	90	90
C17	C18	C19	C20	C21	C22	C23	C24
40	130	130	130	120	115	108	106
C25	C26	C27	C28	C29	C30	C31	C32
42	159	185	120	120	102	90	90

Fine tuning of  $^{19}\text{F}$  mode is achieved by connecting another capacitor in parallel with C6 as shown in Figure 2. When  $^{19}\text{F}$  tuning capacitor CF19T varies from 0 pF to 2000 pF,  $^{19}\text{F}$  resonant peak varies from (188.224 MHz, 14.727 V) to (184.871 MHz, 16.606 V) while  $^1\text{H}$  resonant peak changes only from (200.435 MHz, 13.602 V), which is a clear indication that each mode is independently tuned. The frequency response characteristics of simulation circuit are shown in Figure 3. The figure shows clean,

selective excitations of the individual resonant modes. Simulation assumes a high  $Q$  circuit (very small resistance).

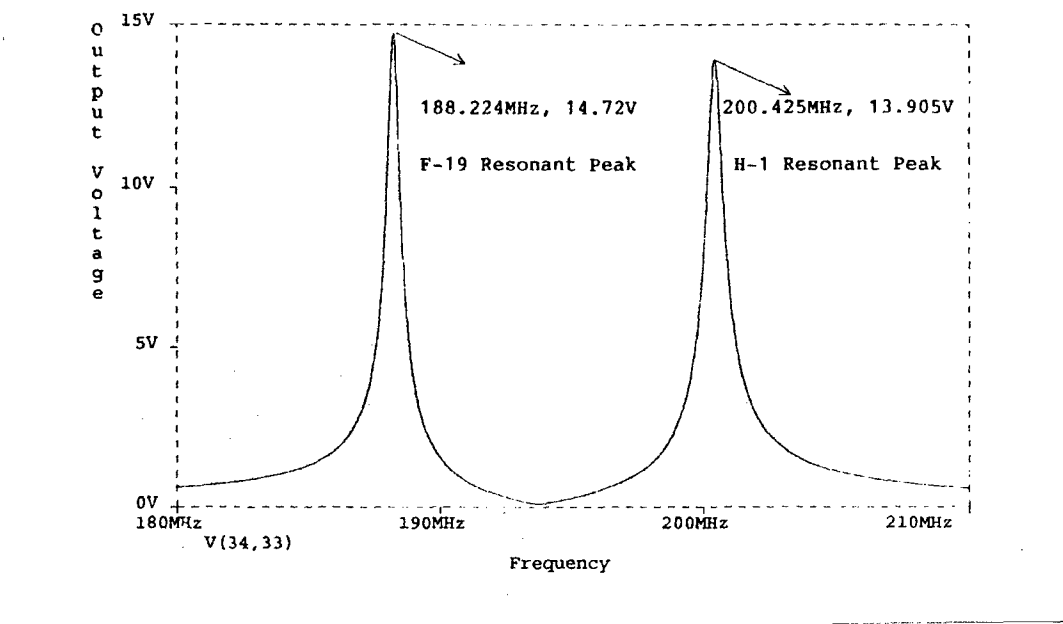


**Figure 3** Frequency response characteristics of the double-tuned birdcage resonator from P-Spice simulation study

### 2.2.3 Construction

A 16-leg high-pass double-tuned birdcage resonator was constructed according to the design principles and the simulation results described above. The resonator is tunable to both 188.2 MHz and 200.1 MHz for operation at  $^{19}\text{F}$  and  $^1\text{H}$  frequencies on a 4.7 T magnet. The cylindrical resonator body is 24.60 cm in length and has an outer diameter of 24.00 cm. The outer structure of the resonator is made of a 5 mm thick plexiglass cylinder, which provides mechanical support and structural stability for the resonator. A 0.2 mm thick copper sheet shield, connected to the ground, is mounted on the inner wall of the outer plexiglass cylinder.

The critical part of the resonator is its inner structure. The inner structure, made from a 5 mm thick plexiglass cylinder, has an outer diameter of 10.50 cm. On the inner wall of the plexiglass cylinder are mounted directly 16 copper sheets (legs) with 1.5 mm gaps and 32 capacitors. The size of the uniform region of  $B_1$  magnetic field generated by the resonator is directly related to the number of legs. The more

numerous the legs, the more uniform the  $B_1$  magnetic field in the radial direction. I chose to build a birdcage resonator with sixteen legs because the  $B_1$  magnetic field generated should, in principle, be uniform enough for my applications and should produce strong NMR signal. The legs are made from 0.1 mm thick copper foil. Each of the sixteen legs is 16.5 cm in length, 1.0 cm in width in the central part and 1.5 cm in width at the two ends (Figure 4).

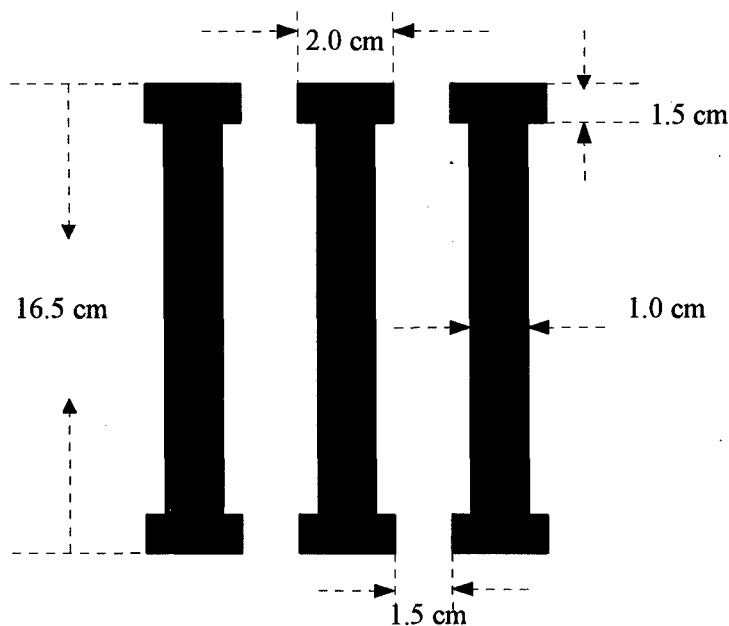


**Figure 4** Geometry of the legs (copper sheets).

The structure of the two end rings, *i.e.*, the two circular bands at the ends of the resonator, consisted of capacitors and was made identical to achieve electrical balance so that the loading effects of the sample could be reduced. The resonator is double-tuned, and is driven between equivalent points on the two rings halfway between two adjacent parallel legs.

The resonator was tuned by individually adjusting the CF19T and CH1T at each of the resonant frequencies. The capacitively coupled tuning loops were placed between legs 11 and 13 and legs 19 and 21 as shown in Figure 2. These loops were connected by standard coaxial cables to the external tuning capacitors CF19T and CH1T that allowed each resonant mode to be independently tuned. Special care was taken to ensure that there was little tuning interaction between the two resonant

frequencies as possible. The resonator was matched capacitively through a variable capacitor  $C_{\text{match}}$ . A photo of the resonator is shown in Figure 5.

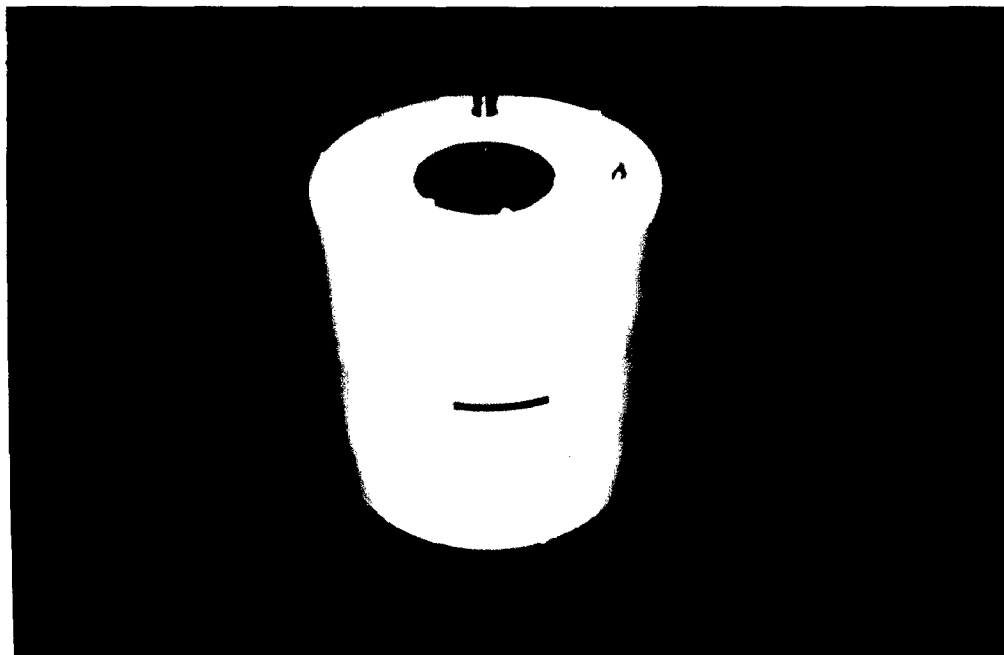


**Figure 5** A photo of the 16-leg double-tuned whole body birdcage resonator.

#### **2.2.4 Bench Testing**

The laboratory bench testing was carried out using a network analyzer (HP8752A). To test the resonator's performance, it was essential to have a set of standard samples that simulated the type of *in vivo* samples used in the magnet. Two NMR phantoms were prepared for this purpose, which roughly had the same loading effects (lowering  $Q$  and shifting resonant frequencies) as a male adult rat ( $\sim 250$  g). A 444 ml phantom was made of a plastic bottle filled with a solution of saline and trifluoroacetic acid (TFA, 5% v/v). A smaller 250 ml phantom, also made of a plastic bottle, was filled with a solution of TFA (5% V/V) and  $\text{CuSO}_4$  (1 g/liter) in distilled water. The major chemical components and the concentrations of the phantoms are listed in Table 2.

The resonator's resonant frequencies, unloaded and loaded  $Q$  values (quality factors) and  $Q$  damping for each of the resonant modes as measured by the network analyzer are presented in Table 3.  $Q_0$  is the unloaded  $Q$  value measured with the resonator in air (without phantom), while  $Q_L$  is the  $Q$  value measured when the saline phantom was placed centrally inside the resonator. The  $Q$  damping is defined as the ratio of  $Q_0/Q_L$ . The results are the means of three measurements. The loaded  $Q$  values are affected by the dimensions of the phantom and its position in the resonator. In general, the loaded  $Q$  values are dominated by the effect of the RF lossy sample. The  $Q$  values decrease as the dimensions of the sample increases.

**Table 2** Major chemical components and the concentrations of the 444 ml saline phantom.

CHEMICAL NAME	CONCENTRATION (g/l)
<i>NaCl</i>	6.90
<i>KCl</i>	0.375
<i>MgSO<sub>4</sub></i>	0.145
<i>CaCl<sub>2</sub></i>	0.185
<i>Na<sub>2</sub>HCO<sub>3</sub></i>	2.10
<i>Glucose</i>	1.80

**Table 3** Results of the laboratory bench testing of the birdcage resonator.  $Q_0$  and  $Q_L$  were measured with the 444 ml phantom.

Resonant Mode	Resonant Frequency (MHz)	Unloaded $Q_0$	Loaded $Q_L$	$Q_0/Q_L$
<sup>19</sup> F	188.22	14	9	1.56
<sup>1</sup> H	200.16	13	8	1.63

It can be seen from Table 3 that the unloaded  $Q_0$ , loaded  $Q_L$ , and the  $Q$  damping  $Q_0/Q_L$  for both resonant modes are similar. The relatively low  $Q$  values may be attributed to the relatively long coaxial cables used to connect the tuning and match circuits. Another possible reason could be the large size of the resonator because the longer the legs, the larger their resistance, causing increased resistance losses and significantly lowering  $Q$  values.



One of the consequences of the low  $Q$  values on the NMR experiments would be to increase the  $90^\circ$  pulse width for a given RF power level. This can be verified by the following equation [4]:

$$PW = K \left( \frac{V_R}{Q} \right)^{1/2} \quad (3)$$

where  $PW$  is the  $90^\circ$  pulse width,  $V_R$  is the resonator volume,  $Q$  is the quality factor of the resonator, and the factor  $K$  is roughly a constant for all resonator designs. This equation indicates that the  $90^\circ$  pulse width is linearly proportional to the square root of resonator's volume and inversely proportional to the square root of resonator's  $Q$  value.

### 2.2.5 Phantom Imaging

The double-tuned birdcage resonator's NMR performance was tested on the Omega CSI 4.7 T superconducting magnet, which operates at a proton frequency of 200.106 MHz and a fluorine frequency of 188.273 MHz. The phantom was centered in the resonator and the resonator was positioned in the isocenter of the magnet, with its axis being aligned with the direction of the magnet's static magnetic field  $B_0$ . The  $90^\circ$  pulse widths were determined from a  $180^\circ$  null of the whole sample. Typical  $90^\circ$  pulse widths were 700  $\mu$ s for proton and 350  $\mu$ s for fluorine. Shimming was accomplished on the water proton FID of the saline solution in the phantom, with the resonator tuned to the double resonant modes. The goal was to obtain a  $B_0$  of homogeneous strength over the entire imaging sample volume. Fourteen shim currents were adjusted on the proton FID through the system automated shimming utility until a symmetrical and long FID was obtained. The proton spectral linewidth at half height after shimming was 34 Hz, which was sufficient for imaging experiments.

To minimize acquisition time, a driven equilibrium spin-echo pulse sequence with a fairly short echo time ( $TE = 8$  ms) was employed so that the  $T_2$  dephasing effects were not significant. Proton transaxial (transverse) images (Figure 6) were acquired as a 3-D data set with a repetition time  $TR = 150$  ms, echo time  $TE = 8$  ms, and a  $128 \times 64 \times 8$  matrix size over  $100 \text{ mm} \times 100 \text{ mm} \times 200 \text{ mm}$  field of view (FOV), providing  $0.78 \text{ mm} \times 1.56 \text{ mm} \times 25 \text{ mm}$  digital resolution. To improve signal-to-noise ratio (SNR), two acquisitions were averaged for each image, thus, giving a total acquisition time of 2 min 33 sec. Proton coronal (Figure 7(A) and (B)) and sagittal images (Figure 7 (C) and (D)) were also acquired with the same imaging parameters except  $FOV = 200 \times 200 \text{ mm}$ .

The signal-to-noise ratios (SNRs) for the images with 2 averages were measured using a standard routine. The values for signal were measured from a randomly chosen portion of images by a square crop and the values for noise were

taken from the four corners of the image background. For each measurement, the square crop covered a reasonably large area of the image or background, so that the data obtained were unbiased. The results of SNR measurements for the proton images are listed in Table 4. The resonator's  $B_1$  field homogeneity was estimated by visual inspection of the images.

**Table 4** Results of SNR measurements for the proton images.

	Upper-Left SNR	Upper-Right SNR	Lower-Left SNR	Lower-Right SNR	Mean SNR	SD
<b>Transaxial Section</b>	88.0	97.4	93.0	93.3	92.9	3.9
<b>Sagittal Section</b>	279.8	272.7	278.7	294.0	281.3	9.0
<b>Coronal Section</b>	287.5	114.3	267.7	125.8	198.8	91.4

The spectrometer frequency was then set on resonance for the  $\text{CF}_3$  group of TFA, without retuning the resonator. The  $90^\circ$  pulse was 360 ms. The  $^{19}\text{F}$  spin-echo images of the 444 ml phantom were acquired as transaxial, sagittal and coronal projections (Figure 8). The images were fluorine density-weighted with  $\text{TR} = 150$  ms and  $\text{TE} = 8$  ms (using driven equilibrium spin-echo pulse sequence) and were averaged 16 times to achieve an acceptable SNR. Thus, each image was acquired in 2 min 33 sec. The image matrix size was  $128 \times 64$  with a field of view of  $100 \times 100$  mm for the transaxial projection and  $200 \times 200$  mm for the sagittal and coronal projections, respectively.

**Table 5** Results of SNR measurements for the  $^{19}\text{F}$  images.

	Upper-Left SNR	Upper-Right SNR	Lower-Left SNR	Lower-Right SNR	Mean SNR	SD
<b>Transaxial Section</b>	3.2	3.3	3.4	3.5	3.3	0.1
<b>Sagittal Section</b>	5.9	6.7	7.3	6.9	6.7	0.6
<b>Coronal Section</b>	4.3	4.5	3.8	3.7	4.1	0.4

The image SNRs were measured in the same way as the proton images and the results are presented in Table 5. The spin-lattice relaxation time  $T_1$  of the  $\text{CF}_3$  group was estimated by applying a non-spatially selective inversion recovery (IR) RF pulse. Seven different IR delays ( $\tau$ ) increasing in the range between 800 ms to 20 sec were used (Table 6). The  $T_1$  value was calculated based on the Levenberg-Marquardt three-parameter fitting algorithm [5] on peak intensity values (Table 6).

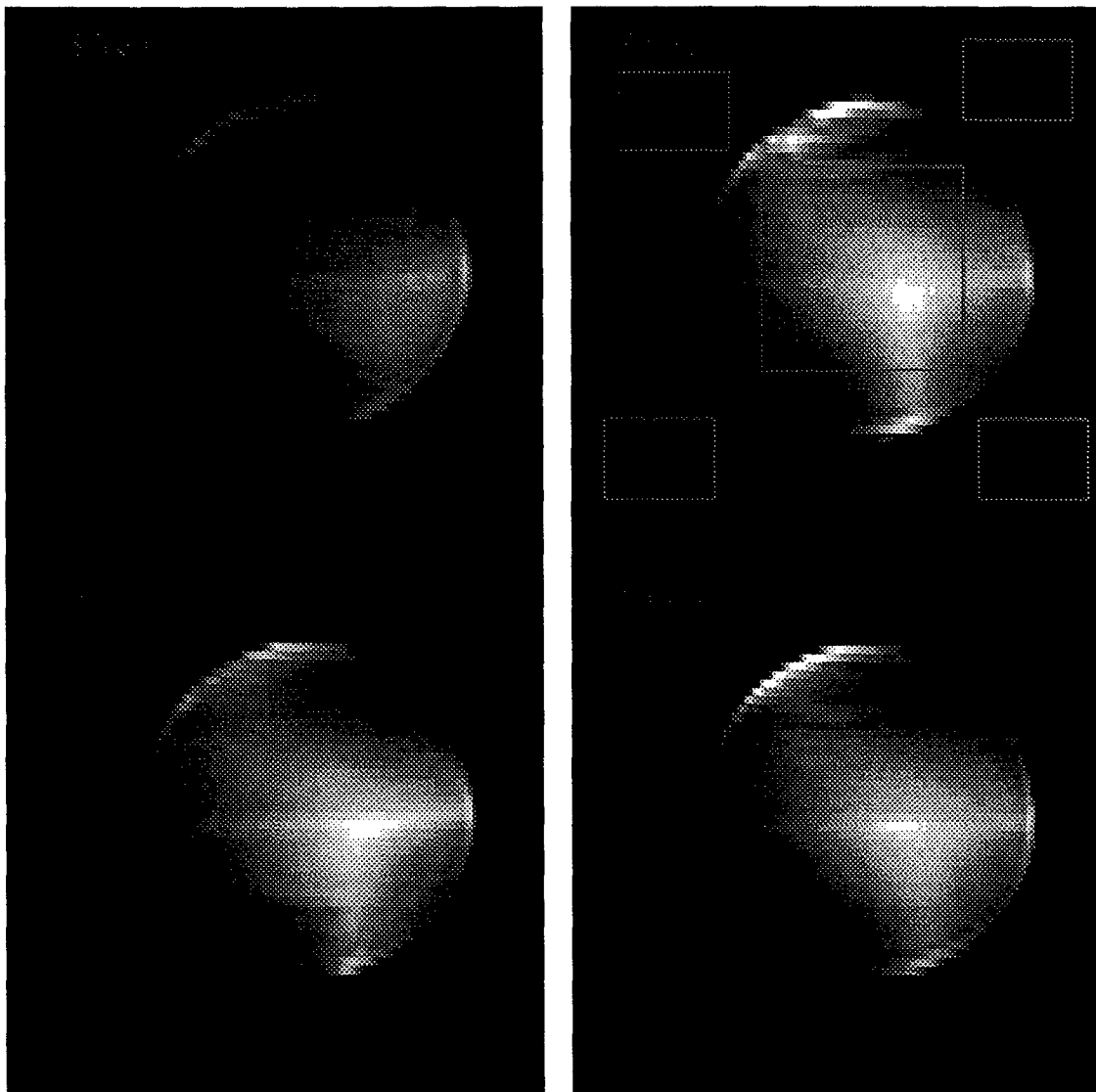


**Figure 6** Proton transaxial images of a 444 ml phantom acquired using a 4.7 T magnet. The images shown are consecutive slices. Imaging parameters: TE = 8 ms, TR = 150 ms, slice thickness = 2.5 cm, NA = 2, FOV = 100 x 100 mm and matrix size = 128 x 64.

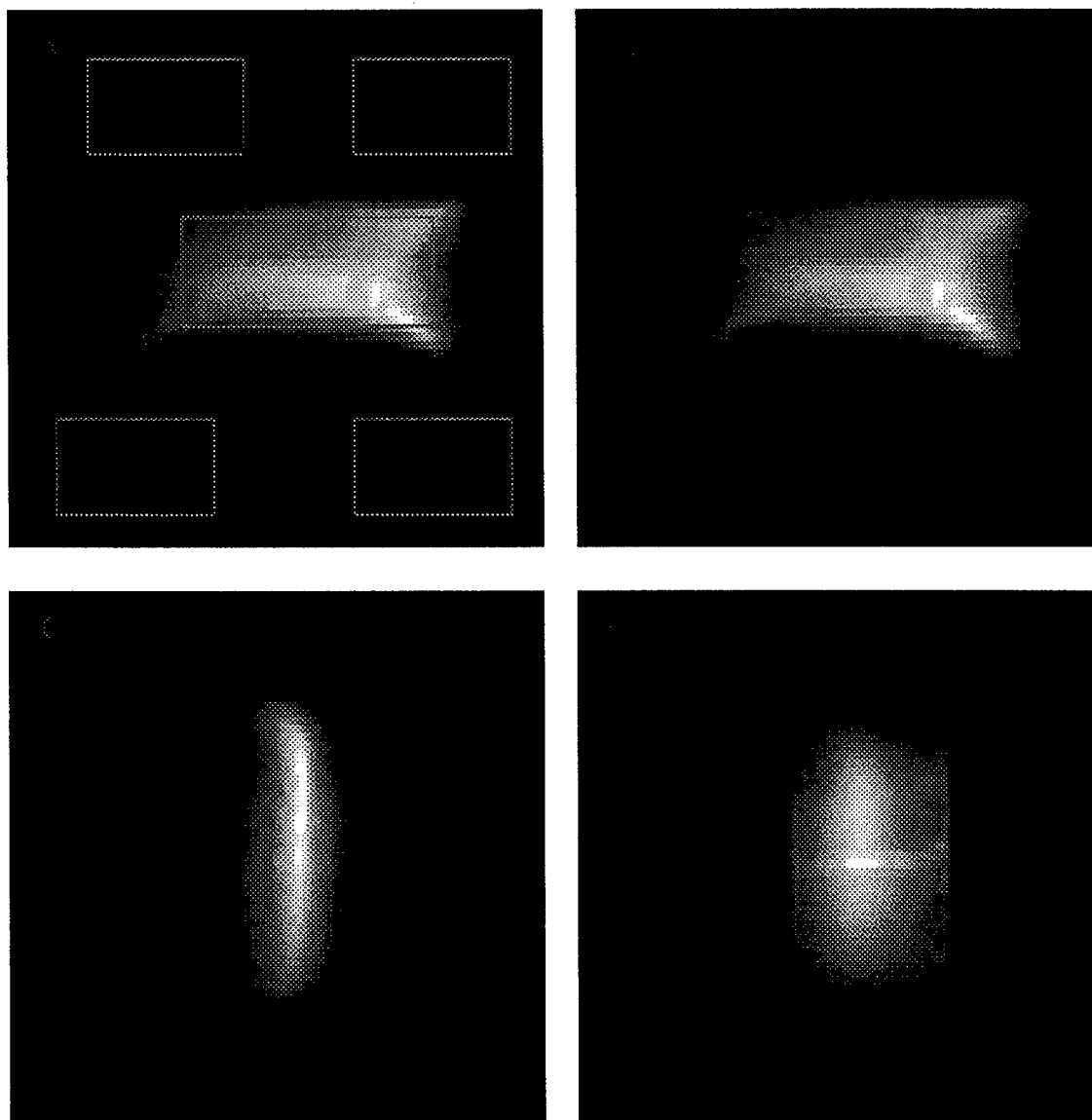


**Figure 7** Proton coronal (A and B) and sagittal (C and D) images of a 444 ml phantom acquired using a 4.7 T magnet. Imaging parameters: TE = 8 ms, TR = 150 ms, slice thickness = 2.5 cm, NA = 2, FOV = 200 x 200 mm and matrix size = 128 x 64.

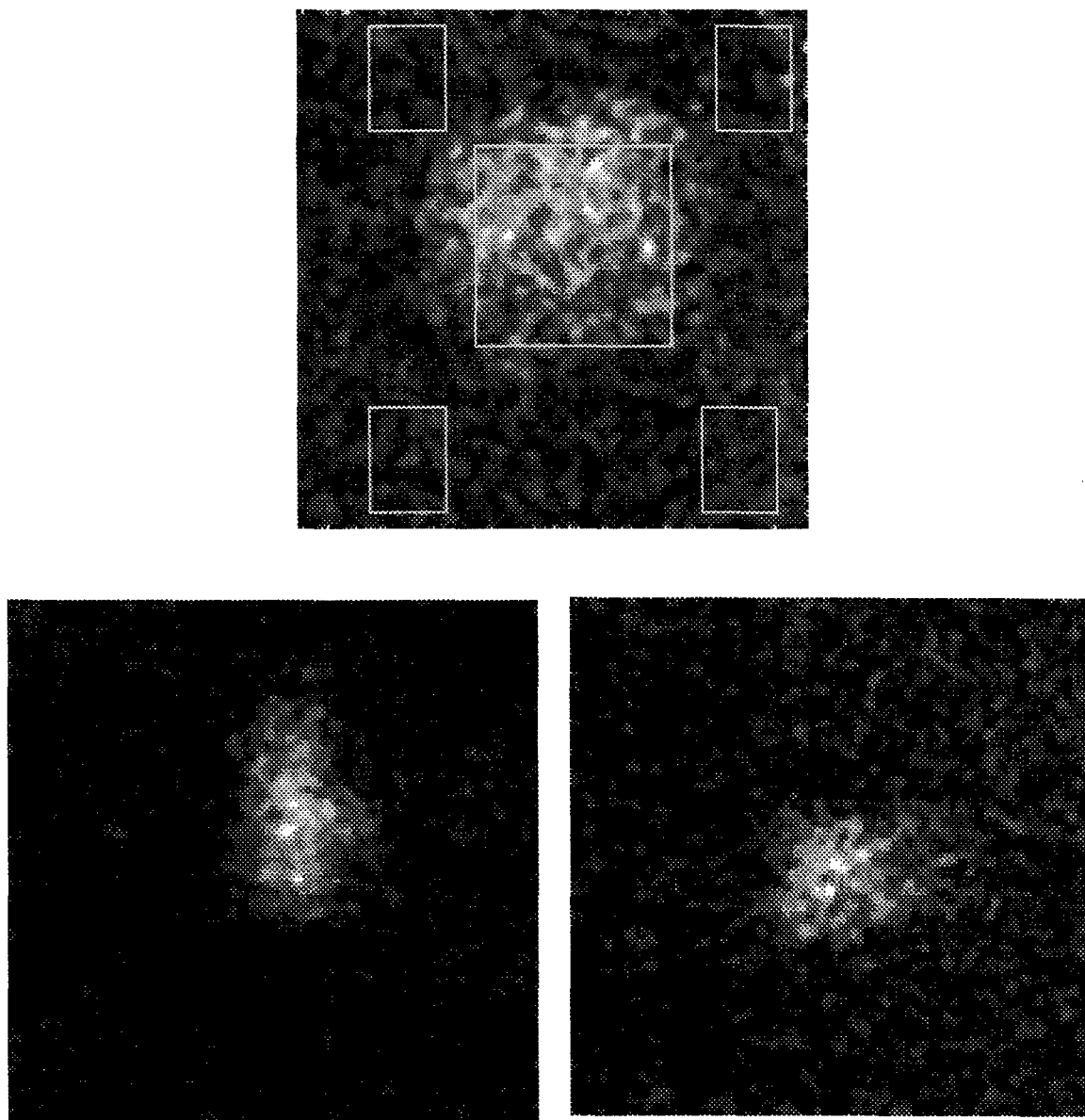


**Figure 8**  $^{19}\text{F}$  MR projection images of a 444 ml phantom. Imaging parameters: TE = 8 ms, TR = 150 ms, NA = 16, FOV = 200 x 200 mm (B and C), FOV = 100 x 100 mm (A) and matrix size = 128 x 64.. A) A transaxial projection image. B) A sagittal projection image. C) A coronal projection image.

**Table 6** Results of T1 measurement for TFA solution and delay list ( $\tau$ ) of the inversion recovery pulse sequence.

$$\text{Function: } y = A \cdot (1 - (W + 1) \cdot \exp(-\tau/T1))$$

$$A = 1.92e+06 \pm 26484$$

$$W = 0.026 \pm 0.042$$

$$T1 = 2.3 \pm 0.19$$

$$\text{Standard Error} = 41129.6$$

$$Y \text{ Standard Deviation} = 31091.1$$

Tau	Intensity	Calc	Diff	#sd
20.000	1923050.524	1923610.434	559.911	0.018
16.000	1932423.278	1921888.260	-10535.018	-0.339
8.000	1857983.273	1859578.430	1595.157	0.051
4.000	1534324.010	1567419.792	33095.782	1.064
2.000	1135584.863	1085041.321	-50543.542	-1.626
1.000	587685.972	637132.244	49446.272	1.590
0.800	545796.816	522178.645	-23618.170	-0.760

### 2.2.6 Discussion

In the past, the complexity of birdcage resonator hindered the application of traditional equivalent circuit analysis [3]. Here, I present a practical approach based on computer simulation to build a 16-leg double-tuned whole body birdcage resonator. The resonator has two resonant frequencies with 188.272 MHz corresponding to  $^{19}\text{F}$  and 200.106 MHz to  $^1\text{H}$ . Laboratory bench testing of the resonator demonstrated that the unloaded  $Q$ s for both proton and fluorine resonant modes are similar and relatively low. The loaded  $Q$  drops by about 36% for fluorine and 39% for proton. The low  $Q$  values mean inefficient use of RF power, which has been verified by the NMR imaging experiments. As a result, this resonator requires the use of a high RF power level that could lead to increased heating of the subject under investigation. One of the possible reasons that limits the  $Q$  value is the use of copper shield intended to shield the sample from electric field interference. In fact, the shield not only lowers the  $Q$  value but also lengthens the pulse width [4].

The  $B_1$  field was found to be somewhat heterogeneous across usable volume of the resonator for  $^1\text{H}$  resonant mode. The  $B_1$  field also exhibited nonuniformity across the phantom for  $^{19}\text{F}$  resonant mode. While this is not so critical for the sagittal and transaxial imaging shown here, it is necessary to increase the RF power level and sacrifice some pulse width to achieve an acceptable  $B_1$  field strength for the coronal

imaging. The  $B_1$  field could be entirely due to the technical difficulty in symmetrically positioning and adjusting the ring capacitances in order to generate an ideal sinusoidal distribution of current around the resonator at the higher frequency. Since sensitivity of the resonator is crucial in the NMR *in vivo* experiments, I believe that the dimensions of the resonator should be minimized in order to obtain an optimal pulse width for the particular subject of investigation.

### 2.3 Slotted Tube Resonator

The slotted-tube resonator was originally developed to efficiently provide  $^1\text{H}$  decoupling to samples in high-field magnets [6]. The common slotted tube resonator consists of a conducting tube with two slots cut symmetrically along both sides of the tube. The surface current distribution produced by the slotted tube resonator peaks near the edges of the conducting tube adjacent to the slots. The conducting tube of the slotted tube resonator is opaque to RF field and diverts all the  $B_1$  field flux through the two slots. Thus, the aperture angle of the slots must be optimized in order for the resonator to generate a homogeneous field. The fundamental feature of the slotted tube resonator is that the conducting component has a low inductance, and hence, large volume resonators can be constructed. At the RF frequencies encountered in clinical MRI systems, this means that the slotted tube resonators can be designed to contain samples of size comparable to that of the human head. The major applications of the slotted tube resonator are for imaging and for localized spectroscopy techniques demanding a uniform flip angle over the entire sample.

#### 2.3.1 Design Theory

The circuit model is illustrated in Figure 9.  $L_s$  and  $R_s$  are sample inductance and resistance, respectively. This circuit model can be further simplified in terms of equivalent circuit (Figure 10) with

$$Z'_2 = \frac{i(L_3 C_3 \omega^2 - 1)}{\omega(C_3 - C_2(L_3 C_3 \omega^2 - 1))} \quad (4)$$

where  $\omega$  is the resonant frequency of the circuit and  $i$  is the imaginary number. Thus, the tuning impedance  $Z_T$  is given by the following expression:

$$\begin{aligned} Z_T &= Z_1 + Z'_2 = \frac{-i}{C_1 \omega} + Z'_2 \\ &= i \frac{C_1(L_3 C_3 \omega^2 - 1) - \omega(C_3 - C_2(L_3 C_3 \omega^2 - 1))}{\omega C_1(C_3 - C_2(L_3 C_3 \omega^2 - 1))} \end{aligned} \quad (5)$$

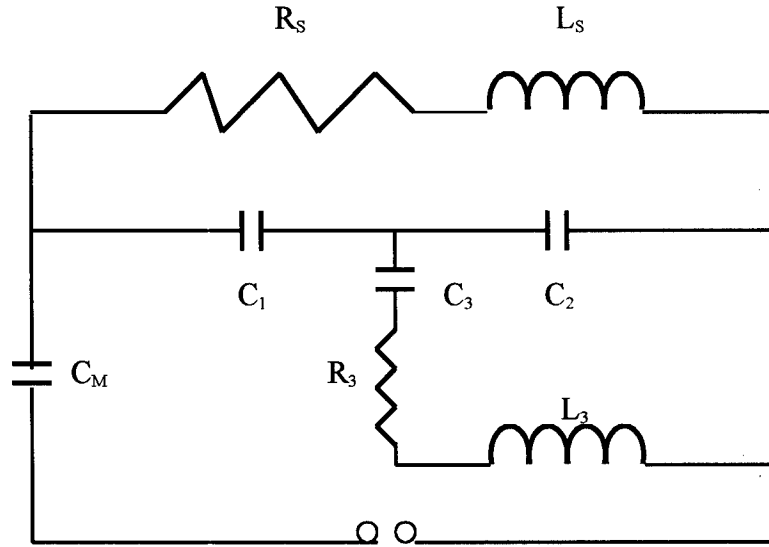


**Figure 9** The circuit model of the switchable slotted tube resonator.  $R_s$  is the sample Resistance and  $L_s$  the sample inductance.  $R_3$  is the equivalent resistance of the tuning loop.

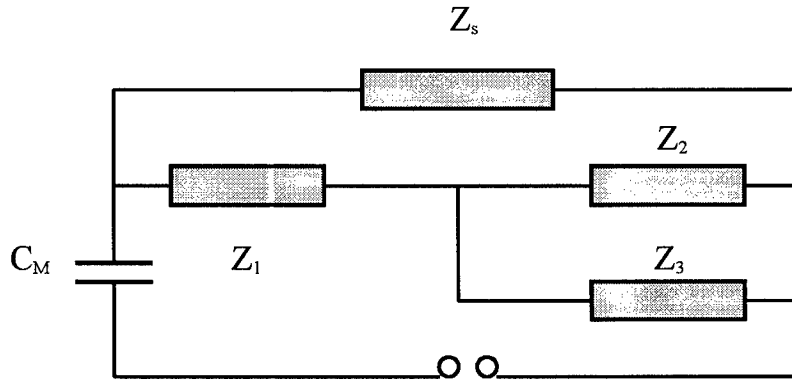


**Figure 10** Equivalent circuit model of the slotted tube resonator.

When the resonator operates at the higher frequency  $\omega = \omega_h$ , the tuning impedance  $Z_T$  is a function of the total capacitance of the tuning circuit and is given by the expression

$$Z_T = -j \frac{(C_1 + C_2')}{\omega_h C_1 C_2'} \quad (6)$$



where

$$C'_2 = \frac{C_2(L_3C_3\omega_h^2 - 1) - C_3}{L_3C_3\omega_h^2 - 1} \quad (7)$$

Thus, the tuning is achieved by adjusting all the capacitors.

When the resonator operates at the lower frequency  $\omega = \omega_1$ , the series  $L_3 C_3$  circuit has a zero impedance and the total tuning impedance is reduced to

$$Z_T = -\frac{i}{C_1\omega_1} \quad (8)$$

Thus, tuning is obtained by adjusting  $C_1$  only.

### 2.3.2 Construction

A switchable slotted tube resonator was constructed based on the above design theory using two copper sheets, which cover an  $80^\circ$  arc [9] for optimal  $B_1$  field homogeneity. The cylindrical resonator body is 23.5 cm long with outer diameter 25.4 cm. The outer structure of the resonator is made of a 5mm thick plexiglass cylinder. The inner structure is made of a 3 mm thick plexiglass cylinder, having a small outer diameter of 7.6 cm to increase the filling factor and reduce the pulse width. The two ends of the resonator are covered by two 6 mm thick plexiglass boards stabilized by 6 nonmagnetic screws on each end, respectively. The two boards, along with the outer structure, provide very stable mechanical support for the resonator. Three capacitors of 20.0 pF were positioned symmetrically between the guard rings and the copper sheets to obtain uniform surface current distribution.

The resonator has a usable length of 15.5 cm, sufficient for *in vivo* adult rat NMR experiments. The two guard rings and two copper sheets are made from 0.3 mm thick copper foil. The width of each of the guard rings is 1.0 cm and there is a spacing of approximately 0.5 cm between the guard ring and the vertical copper sheets, which are joined with capacitors. The copper sheets have a length of 12.5 cm and their width covers about  $80^\circ$ . The resonator is tunable to  $^{19}\text{F}$  (188.22 MHz) and  $^1\text{H}$  (200.16 MHz), and is driven between one copper sheet and one guard ring.

The tuning of the resonator was achieved by three variable capacitors  $C_1$ ,  $C_2$  and  $C_3$ , which are V2145H family high  $Q$  RF capacitors (Voltronics Corporation,

Denville, New Jersey).  $C_1$  and  $C_2$  (NMTM38GE) have a capacitance range of 1.0 ~ 38.0 pF,  $C_3$  (NMTM120CE) has a capacitance range of 2.0 ~ 120.0 pF, and  $C_M$  (NMQM22GE) has a capacitance range of 1.0 ~ 22.0 pF.  $^{19}\text{F}$  resonance was obtained by adjusting  $C_1$  and  $^1\text{H}$  resonance was achieved by adjusting  $C_1$ ,  $C_2$ , and  $C_3$ , respectively. The resonator was matched capacitively through  $C_M$ . A photo of the resonator is shown in Figure 11.

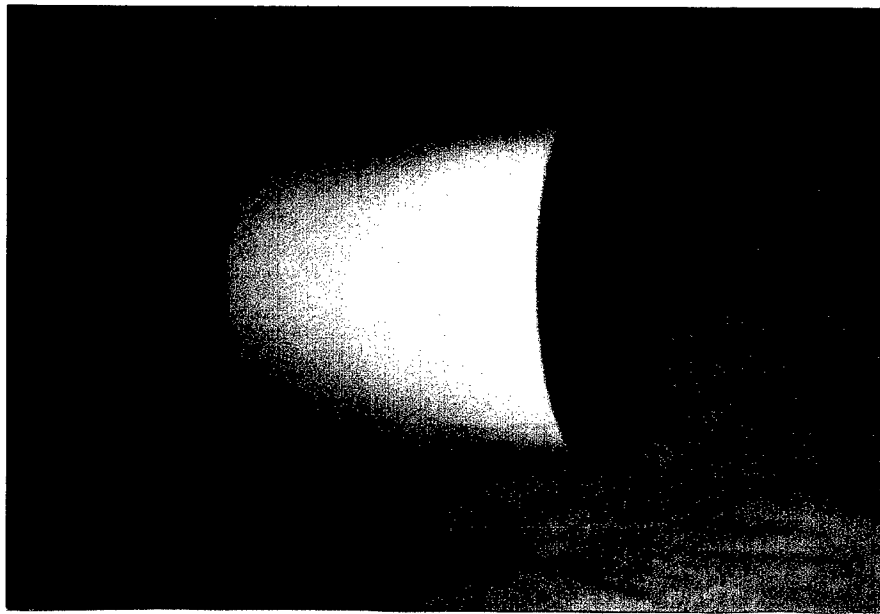


**Figure 10** A photo of the slotted tube whole body resonator.

### 2.3.3 Bench Testing

The resonator was tuned and matched on the laboratory bench with the help of a network analyzer (HP8752A). The unloaded and loaded  $Q$  values were measured with the aid of the network analyzer from the full width at half height of the resonance when the resonator was perfectly tuned and matched.

The resonant frequencies, unloaded  $Q_0$  and loaded  $Q_L$  values and  $Q$  damping for each of the resonant modes are presented in Table 7.  $Q_0$  is the unloaded  $Q$  value measured with the resonator in air (without phantom), while  $Q_L$  is the  $Q$  value measured when the phantom was placed centrally inside the resonator. The  $Q$  damping is defined as the ratio of  $Q_0/Q_L$ . The results are the means of three measurements.

**Table 7** Results of the laboratory bench testing of the slotted tube resonator.  
 $Q_0$  and  $Q_L$  were measured with the 250 ml phantom.

Resonant Mode	Resonant Frequency (MHz)	Unloaded $Q_0$	Loaded $Q_L$	$Q_0/Q_L$
$^{19}\text{F}$	188.22	97.5	54.2	1.80
$^1\text{H}$	200.16	63.8	53.6	1.19

As can be seen from Table 7, the unloaded  $Q_0$  for  $^{19}\text{F}$  is much higher than that for  $^1\text{H}$  1.5 times), and the loaded  $Q_L$  for both resonant frequencies is essentially same. The  $Q$  damping,  $Q_0/Q_L$ , for  $^{19}\text{F}$  is 1.5 times higher than that for  $^1\text{H}$ . This means that the RF lossy phantom has a much stronger effect on the  $^{19}\text{F}$  resonance than on the  $^1\text{H}$  resonance. The high  $Q$  values could be the result of several factors, including a relatively small usable volume, minimized length of connecting wires, and a structure without a copper shield. The high  $Q$  values guarantee that the resonator has a higher excitation efficiency, *i.e.*, the  $90^\circ$  pulse width for a given RF power level is short or the magnitude of the  $B_1$  field generated with a given RF power level is high. The results of the laboratory bench testing also indicated that the resonator was easy to tune and match and both resonant frequencies were stable and immune to external electromagnetic interference.

#### 2.3.4 Phantom Imaging

The NMR performance of the slotted tube resonator was tested on the Omega CSI 4.7 T superconducting horizontal bore magnet operating at a proton resonant frequency of 200.106 MHz and a fluorine resonant frequency of 188.273 MHz. The *in vitro* resonator sensitivity for proton and fluorine was determined using the 250 ml phantom, which was filled with a solution of TFA (5%v/v) and  $\text{CuSO}_4$  (1g/liter) in distilled water.

Measurements of  $90^\circ$  pulse width were performed from a  $180^\circ$  null of the whole sample. Typical  $90^\circ$  pulse widths were around 170  $\mu\text{s}$  for proton and 110  $\mu\text{s}$  for fluorine. Shimming was performed on the water proton FID of the saline solution in the phantom with resonator tuned to the  $^1\text{H}$  resonance, to a typical spectral linewidth of 32 Hz. The driven equilibrium spin-echo pulse sequence was used for the imaging experiment. Imaging parameters were: repetition time  $\text{TR} = 150\text{ms}$ , echo time  $\text{TE} = 8\text{ms}$ , with a data set of  $128 \times 64 \times 8$  with 128 real and 128 imaginary data points, 64

phase encoding steps, and 8 slices. The field of view (FOV) was 80 mm x 80 mm for transaxial images, 100 mm x 100 mm for coronal, and 200 mm x 200 mm for sagittal images. The images were acquired with one excitation, thus giving a total acquisition time of 1.16 min (Figures 12, 13, 14, and 15). The image signal-to-noise ratios (SNRs) were measured as described before. The results of SNR measurements for the proton images are listed in Table 8.

**Table 8** Results of SNR measurements for the proton images.

	Upper-Left SNR	Upper-Right SNR	Lower-Left SNR	Lower-Right SNR	Mean SNR	SD
<b>Transaxial Section</b>	389.3	199.5	897.8	666.3	538.2	177.1
<b>Sagittal Section</b>	494.2	517.5	478.8	450.5	485.3	28.1
<b>Coronal Section</b>	190.3	30.2	164.6	22.8	102.0	87.9

Following the  $^1\text{H}$  imaging experiment, the resonator was retuned in place to 188.27 MHz and corresponding  $^{19}\text{F}$  imaging experiment was carried out. The  $90^\circ$  pulse was 108  $\mu\text{s}$  and the spectral linewidth after shimming was 46 Hz. The spin-echo (SE) images were acquired with the imaging parameters: TR = 150 ms, TE = 8 ms, FOV = 100 x 100 mm, NA = 16, and matrix size = 64 x 32. Figure 16 shows four fluorine SE transaxial images. Figure 17 (A) shows a proton transaxial EPI image and Figure 17 (B) shows the corresponding fluorine EPI image of the same phantom. The image SNR measurements were performed in the same way as the proton images and the results are given in Table 9.

**Table 9** Results of SNR measurements for the fluorine images.

	Upper-Left SNR	Upper-Right SNR	Lower-Left SNR	Lower-Right SNR	Mean SNR	SD
<b>Transaxial Section</b>	3.1	2.9	2.6	3.0	2.9	0.2
<b>Sagittal Section</b>	4.2	5.1	4.0	4.2	4.4	0.5
<b>Coronal Section</b>	4.2	4.3	4.7	4.6	4.5	0.2

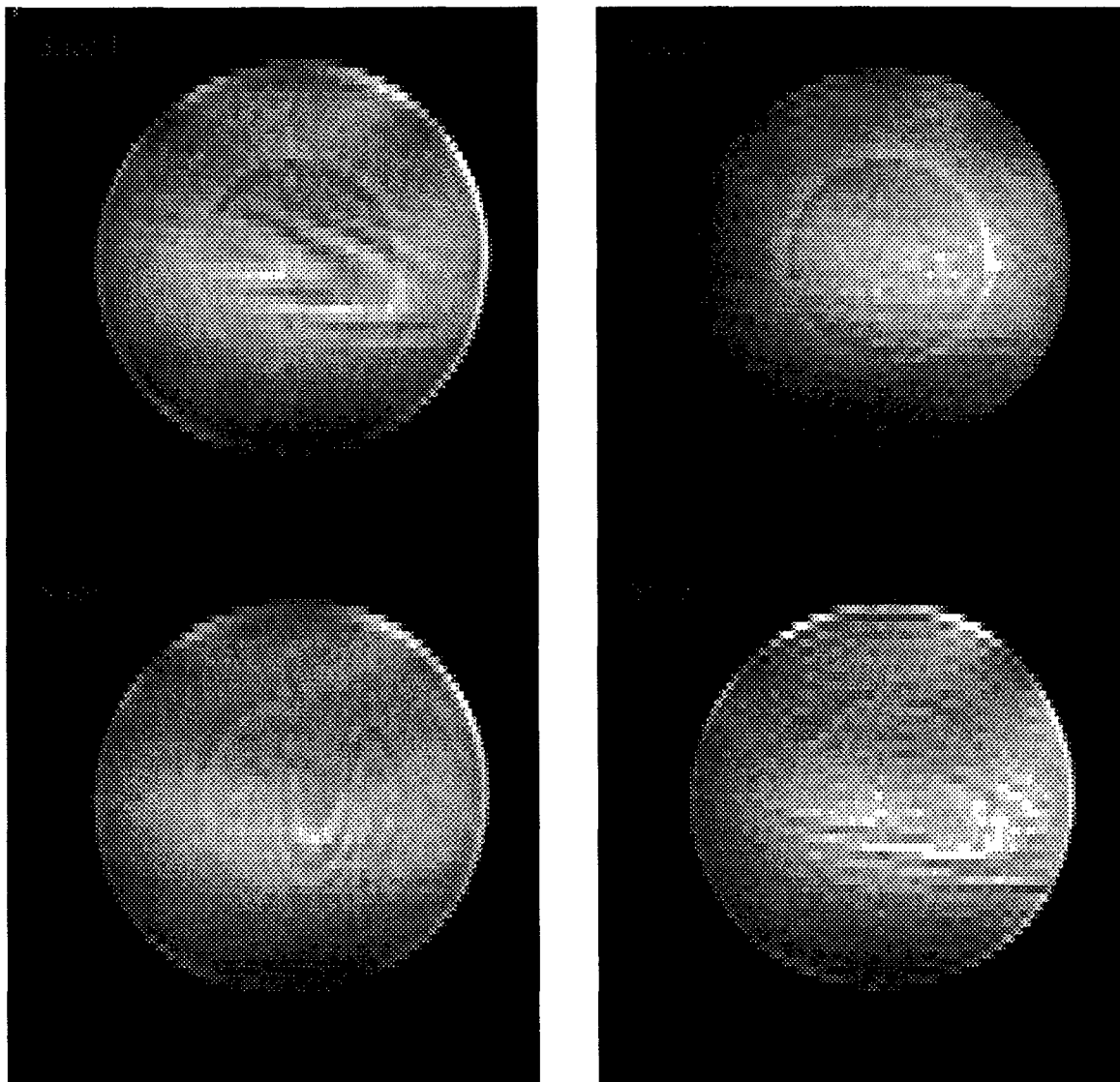


**Figure 12** Proton transaxial images of a 250 ml phantom acquired using a 4.7 T magnet. The images shown are the first 4 slices. Imaging parameters: TE = 8 ms, TR = 150 ms, slice thickness = 12.5 mm, NA = 1, FOV = 80 x 80 mm and matrix size = 128 x 64.

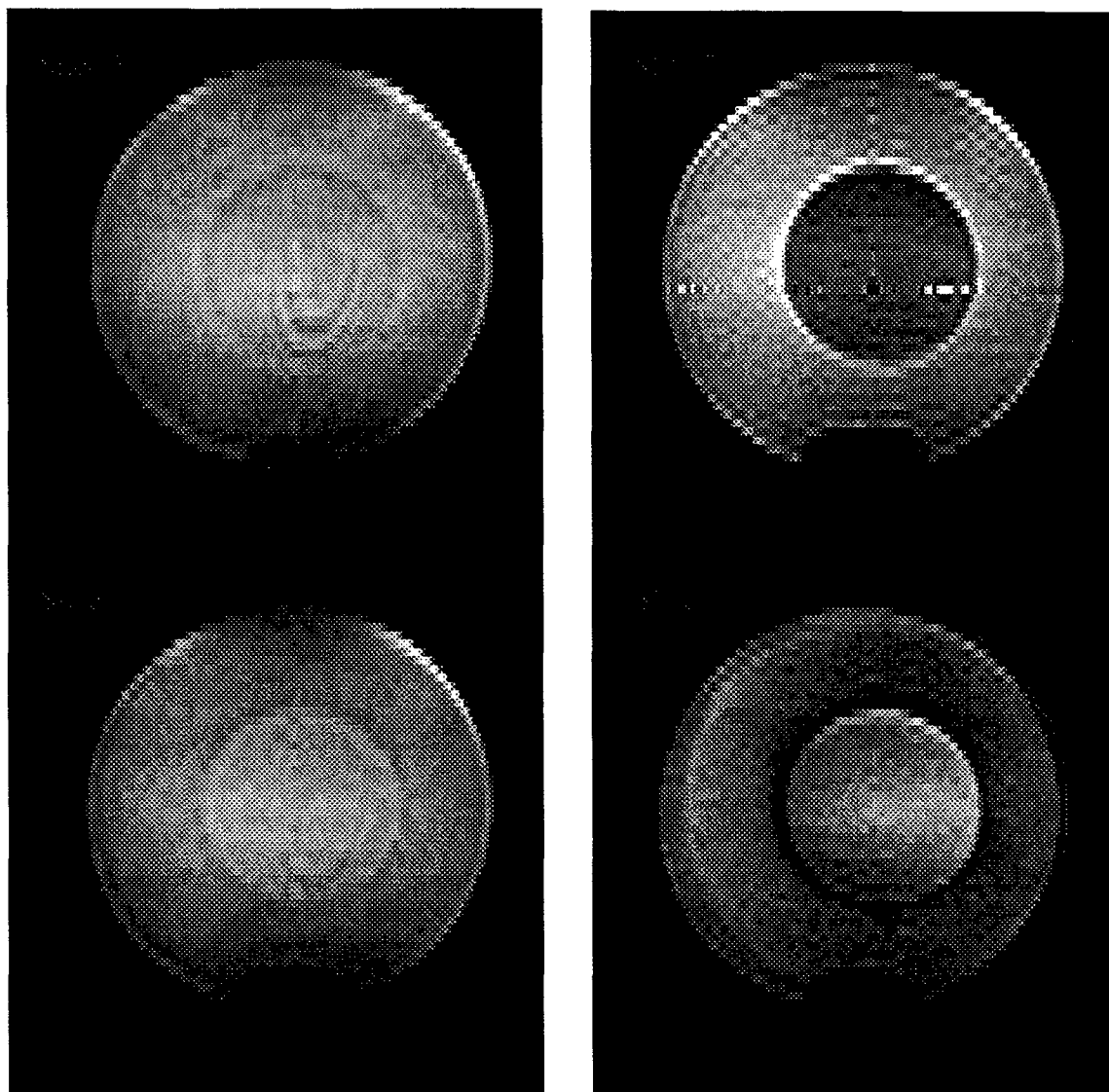


**Figure 13** Proton transaxial images of a 250 ml phantom acquired using a 4.7 T magnet. The images shown are the last 4 slices. Imaging parameters: TE = 8 ms, TR = 150 ms, slice thickness = 12.5 mm, NA = 1, FOV = 80 x 80 mm and matrix size = 128 x 64.

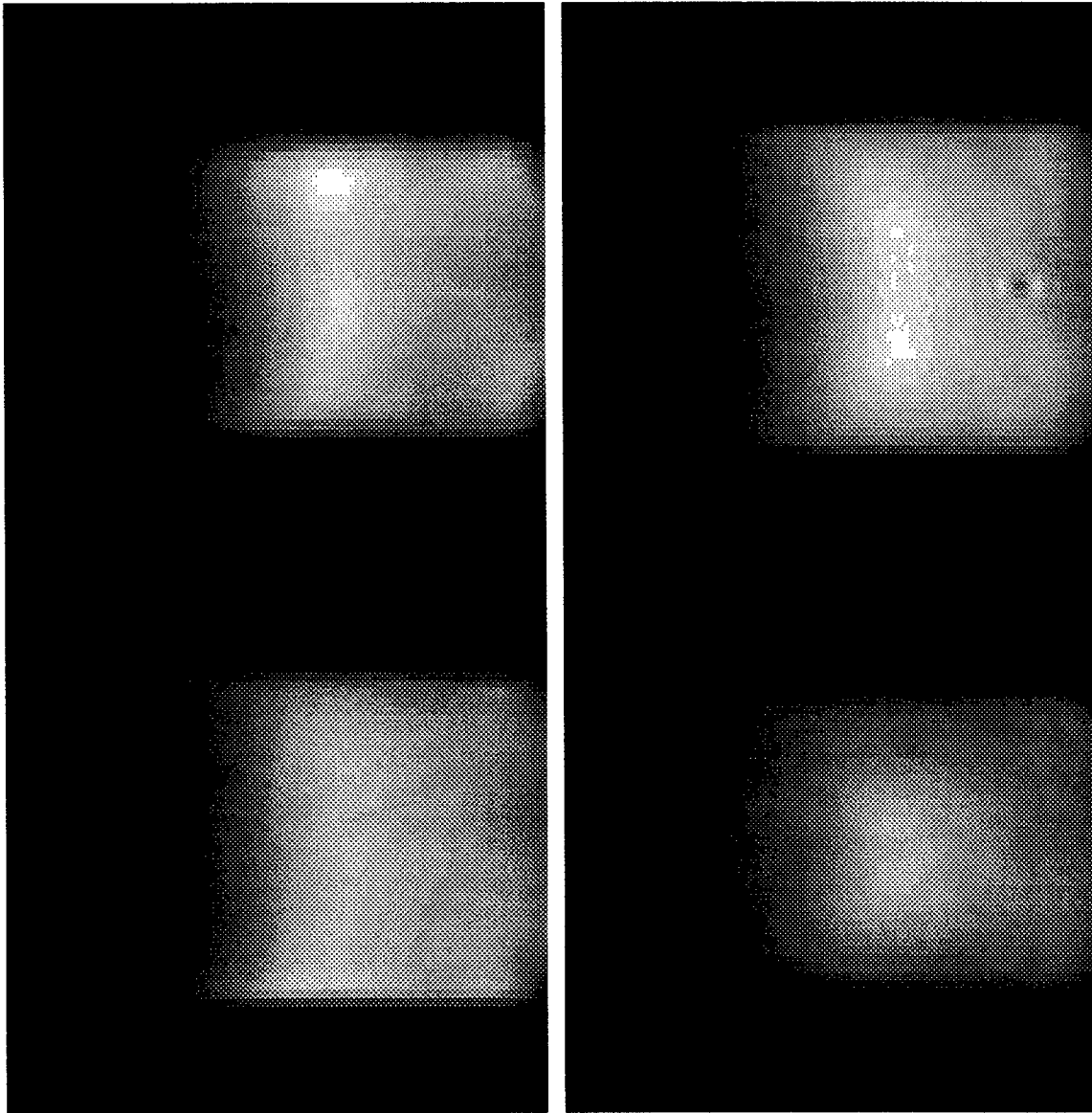


**Figure 14** Proton coronal images of a 250 ml phantom acquired using a 4.7 T magnet. The images shown are the middle 4 slices. Imaging parameters: TE = 8 ms, TR = 150 ms, slice thickness = 10 mm, NA = 1, FOV = 100 x 100 mm and matrix size = 128 x 64

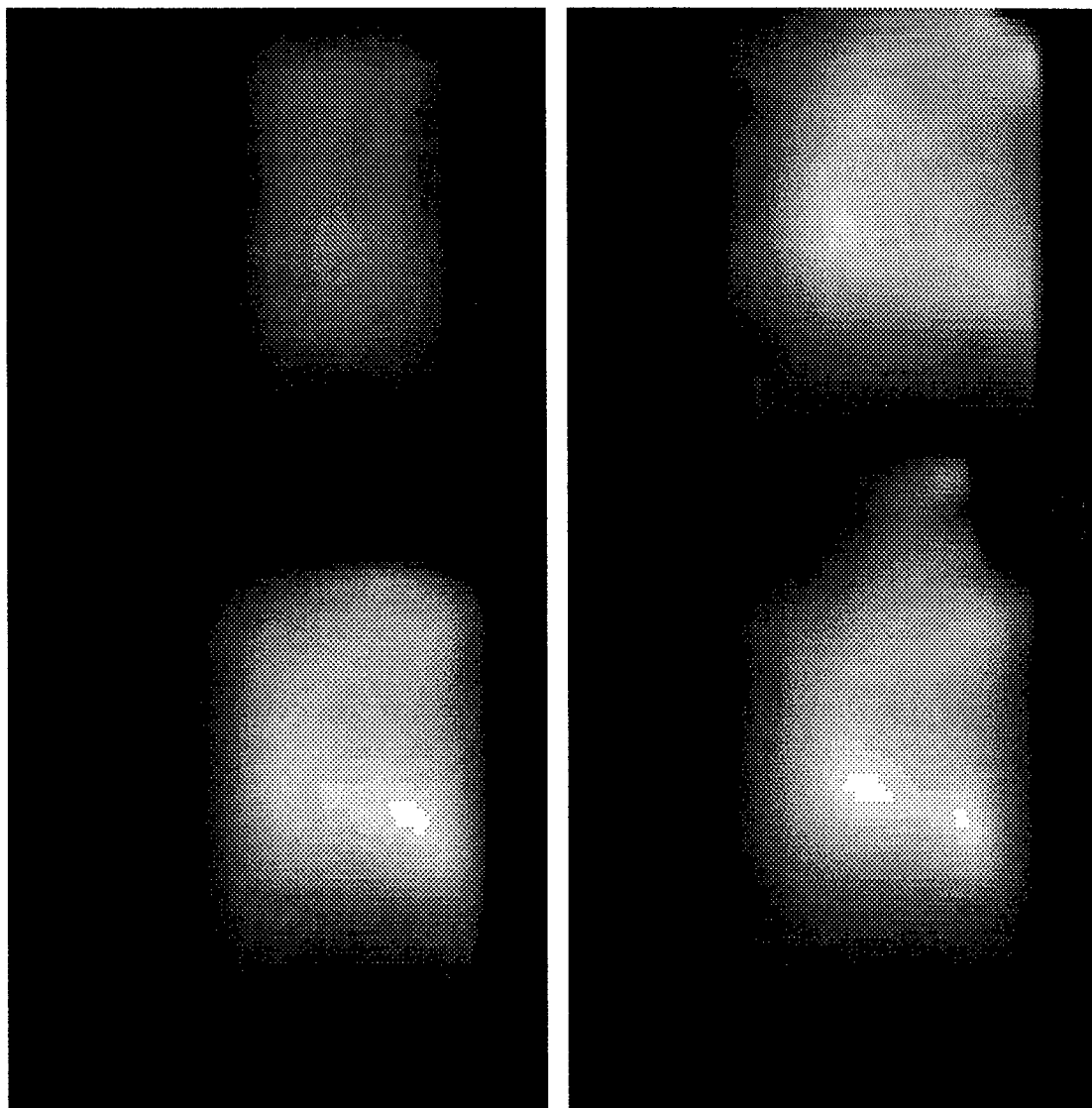


**Figure 15** Proton sagittal images of a 250 ml phantom acquired using a 4.7 T magnet. The images shown are the middle 4 slices. Imaging parameters: TE = 8 ms, TR = 150 ms, slice thickness = 10 mm, NA = 1, FOV = 200 x 200 mm and matrix size = 128 x 64



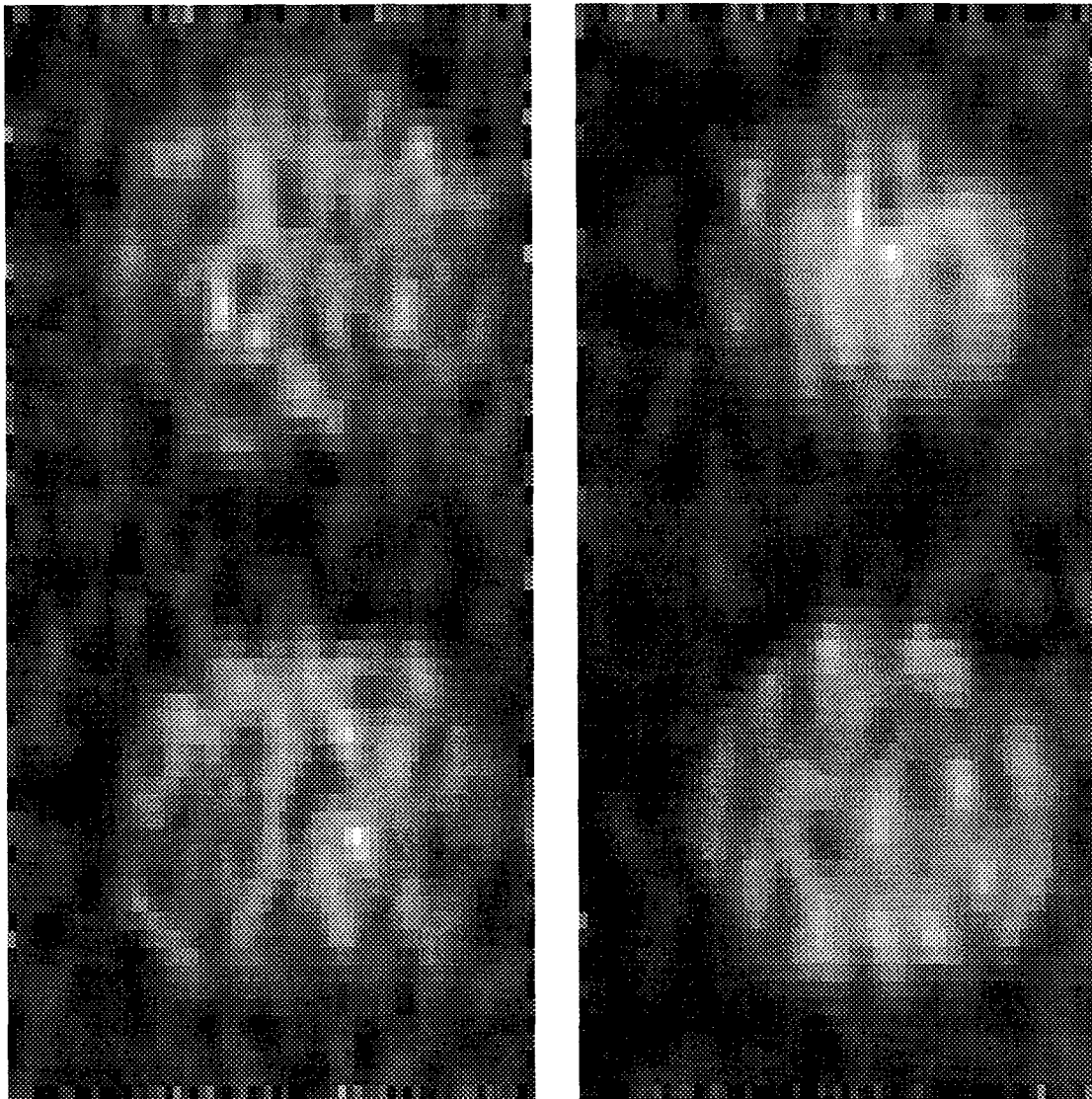
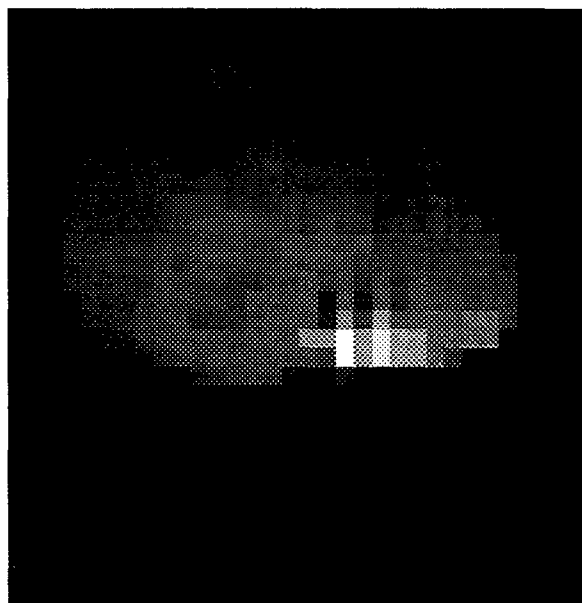


**Figure 16** Fluorine transaxial images of a 250 ml phantom acquired using a 4.7 T magnet. The images shown are the middle 4 slices. Imaging parameters: TE = 8 ms, TR = 150 ms, slice thickness = 10 mm, NA = 16, FOV = 80 x 80 mm and matrix size = 64 x 32

A



B

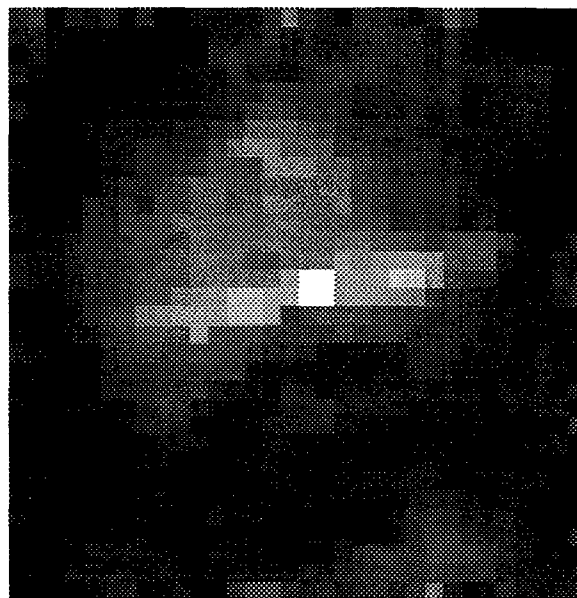


**Figure 17** A) A proton transaxial EPI image of a 250 ml phantom acquired using a 4.7 T magnet. B) A fluorine transaxial EPI image of the same phantom. Imaging parameters: TE = 8 ms, TR = 1500 ms, slice thickness = 10 mm, NA = 1 ( $^1\text{H}$ ), NA = 4 ( $^{19}\text{F}$ ), FOV = 80 x 80 mm and matrix size = 32 x 32

### 2.3.5 Discussion

A theoretical approach to design a swithable slotted-tube resonator was presented. The resonator has the capability of being continuously tuned in the frequency range of 150 MHz ~ 220 MHz. At each particular frequency, a sharp resonance can be easily obtained with tuning and matching circuits. The resonator has high  $Q$  values and short  $90^\circ$  pulse widths for both proton and fluorine, which results in improved sensitivity and makes *in vivo* tumor  $pO_2$  studies possible.

A comparison between Tables 4 and 8, and Tables 5 and 9 indicates that the  $^1H$  SNRs for the slotted tube resonator are about 3 times higher than those for the birdcage resonator and the  $^{19}F$  SNRs are virtually same for the both resonators. Several possible reasons could cause this discrepancy. First of all, the slotted tube resonator has a higher filling factor and less resistance loss than the birdcage resonator, and these would enhance the RF transmitting efficiency. Secondly, the slotted tube resonator used the small phantom for the SNR measurements and hence, the amount of energy received per nucleus was higher than that for the large phantom for a given RF power. These two reasons could result in higher  $^1H$  SNRs for the slotted tube resonator. As to the relatively low  $^{19}F$  SNRs for the slotted tube resonator, this could be entirely due to the low fluorine nucleus concentration in the small phantom solution. Another thing worth mentioning here is that when acquiring EPI images, the 1 kW amplifier had to be tuned on in order to get strong  $^{19}F$  signals for both resonators.

The  $B_1$  field homogeneity was found to be excellent for proton resonance and reasonably good for fluorine resonance across the usable volume of the resonator. The  $B_1$  field homogeneity was sufficient for this project.

### 3. Software Development

#### 3.1 Program to Assess the Goodness of T1 Relaxation Curve Fit

EPI is used as a basic building block and combined with additional spin preparation sequences. To measure spin-lattice relaxation time (T1) and hence  $pO_2$  map, a pulse burst saturating (PBSR) pulse train is applied immediately prior to the EPI sequence. This leads to some loss of dynamic range in the results, but substantially shortens the time required for a T1 experiment and thus, improves the temporal resolution. Fourteen data sets are acquired with delay time in a geometric progression ranging from 200 ms to 90 sec. Since the longest and shortest delays are alternated during data acquisitions to reduce systematic bias, it is necessary to restore the images to the correct order, *i.e.*, from the shortest to the longest delay (200 ms  $\cdots \rightarrow$  90 sec) prior to the curve fit

In order to obtain the spatial distribution (map) of  $pO_2$  in breast tumor, we have to solve for the R1 map of injected HFB first. This is done by fitting each voxel of the fourteen images to a three parameter exponential relaxation model:

$$\begin{aligned} y_n(i, j) &= A(i, j) \cdot [1 - (1 + W) \cdot \exp(-R1(i, j) \cdot \tau_n)] \\ &\quad (n = 1, 2, \dots, 14) \\ &\quad (i, j = 1, 2, \dots, 32) \end{aligned} \tag{9}$$

by the Levenberg-Marquardt least-squares algorithm, where  $y_n(i, j)$  is the measured signal intensity corresponding to delay time  $\tau_n$  ( $n$ th image) for voxel  $(i, j)$ ,  $A(i, j)$  is the fully relaxed signal intensity amplitude of voxel  $(i, j)$ ,  $W$  is a dimensionless scaling factor allowing for imperfect signal conversion, and  $R1(i, j)$  is the relaxation rate of voxel  $(i, j)$  in unit of  $\text{sec}^{-1}$ .

Good T1 relaxation curve fit is crucial in  $^{19}\text{F}$  PBSR-EPI oximetry. It is relatively easy to obtain excellent curve fits, provided  $\text{SNR} > 10$  for most intense signals. To assess the goodness of curve fit, I wrote a Unix based NMR-shell script program to display the T1 relaxation curve of individual voxels of PBSR-EPI images. The graphical representation of the data, relaxation model, and goodness of fit provides a quick and convenient way of assessing the quality of the data. Based on the rms error of fit, the goodness of curve fit can be classified into three categories: good, intermediate, and poor.

For typical good relaxation data, the global least squares minimization is achieved with a very small rms error. These data, related to strong  $^{19}\text{F}$  signal, represent those voxels within the region of interest (ROI). For typical intermediate data, the global least squares minimization is achieved with a relatively large rms error due to a signal bad data point, which could lead to a big T1 error. To improve the relaxation curve fit, a threshold is applied to the raw data, which eliminates those data points  $\geq 3\sigma$  from the curve. The remaining data, thus, provide a better curve fit. In applying the threshold, only one data point is eliminated from the raw data per curve. These relaxation data represent those voxels within the ROI, but have relatively strong  $^{19}\text{F}$  signals. In general, they give good T1 values. For poor relaxation data, the global least squares minimization either fails or converges slowly with a very large rms error. These relaxation data, associated with those voxels outside the ROI, represent either very weak  $^{19}\text{F}$  signals or background noise. They give unreliable T1 values.

### 3.2 Program to Compute HFB Clearance Rate Map

In contrast to traditional PFCs, which exhibit excessive tissue retention, HFB clears from tissue relatively rapidly. Since HFB is a non-ionic freely diffusable tracer, clearance will provide an indication of relative breast tumor blood flow. To compute the HFB clearance rate map, I use a single parameter exponential decay model:

$$Q_{i,j}(t) = Q_{i,j}(0)\exp(-t/T_{i,j}) \quad (10)$$

where  $Q_{i,j}(t)$  is the signal intensity for voxel  $(i, j)$  at time  $t$ ,  $Q_{i,j}(0)$  is the signal intensity for voxel  $(i, j)$  at time zero, and  $T_{i,j}$  is the clearance rate of voxel  $(i, j)$ . In practice, however, Equation (10) is transformed into a logarithmic form:

$$\ln(Q_{i,j}(t)) = \ln(Q_{i,j}(0)) - t/T_{i,j} \quad (11)$$

Based on above theory, I wrote a Unix based NMR-shell script program, which computes the clearance rate  $T_{i,j}$  of individual voxels by fitting the signal intensity of PBSR-EPI images to Equation (11). A clearance rate map is then produced by displaying  $T_{i,j}$  as a color-coded image. This program is capable of determining the global and regional clearance rate of HFB. Source code of the program is provided in Appendix.

## 4. Conclusions

The construction of high quality RF resonators and development of two important programs have established a solid foundation for this project and made monitoring global and regional breast tumor oxygenation using  $^{19}\text{F}$  MRI of HFB possible. PBSR-EPI oximetry of HFB will provide important insights into breast tumor physiology and therapy. I am currently analyzing tumor oxygenation data using these two programs and the results will be available soon.

## 5. References

1. P. M. Joseph and J. E. Fishman, "Design and evaluation of a radio frequency coil for nuclear magnetic resonance imaging of fluorine and proton", *Med. Phys.*, 12:679 - 683, 1985.
2. C. E. Hayes, W. A. Edelstein, J. F. Schenck, O.M.Mueller, and M. Eash, "An efficient, highly homogeneous radiofrequency coil for whole-body NMR imaging at 1.5 T", *J. Magn. Reson.*, 63:622 - 628, 1985.
3. R. Pascone, T. Vullo, J. Farrelly, and P. T. Cahill, "Explicit treatment of mutual inductance in eight-column birdcage resonators", *Magn. Reson. Imag.*, 10:401 - 410, 1992.
4. T. A. Cross, S. Muller and W. P. Aue, "Radiofrequency resonators for high-field imaging and double-resonance spectroscopy", *J. Magn. Reson.*, 62: 87 - 98, 1985.
5. W. H. Press, S. A.. Teukolsky, W. T. Vetterling, and B. P. Flannery, *Numerical Recipes in C*, Cambridge University Press, 683 - 688, 1994.
6. H. J. Schneider, P. Dullenkopf, "Slotted tube resonator: a new NMR probe head at high observing frequencies", *Rev. Sci. Instrum.*, 48:68 - 73, 1977.
7. A. Leroy-Willig, L. Taquin, and M. Sauzade, "The slotted cylinder: an efficient probe for NMR imaging", *Magn. Reson. Med.*, 2:20 - 28, 1985.
8. R. E. Gordon and W.E. Timms, "An improved tune and match circuit for  $B_0$  shimming in intact biological samples", *J. Mag. Reson.*, 46:332 - 324, 1982.
9. D. W. Alderman and D. M. Grant, "An efficient decoupler coil design which reduces heating in conductive samples in superconducting spectrometers", *J. Mag. Reson.*, 36:447 - 451, 1979.

## 6. Appendix

## 6.1 Source code to Compute HFB Clearance Rate Map

```
# Omega Sourceable Script
# File: clearance_rate
# Subprograms called: clearance_rate_sub1 and clearance_rate_sub2
# Author: Yulin Song
# Status: OK
# Time: June 1998

onintr quit
clear
bigwin
clear

@ choice = 1
while (($choice == 1)||($choice == 2)||($choice == 3)||($choice == 4))
    echo ""
    echo ""
    echo ""
    echo ""
    echo ""
    echo ""
    echo ""
    echo ""
    echo ""
    echo ""
    echo ""
    echo "
                                CLEARANCE RATE COMPUTATION PROGRAM
    echo ""
    echo "
                                MAIN MENU
    echo "
    echo ~~~~~~
    echo |
    echo |      1. Purposes of the Program
    echo |
    echo |      2. Usage of the Program
    echo |
    echo |      3. Display T Fitting Curve
    echo |
    echo |      4. Generate T Maps
    echo |
    echo |      5. Exit
    echo |
    echo |
    echo ~~~~~~
    echo ""
```





```

echo " | "
echo " ===== "
echo ""
echo ""
echo ""
echo ""
echo ""
echo ""
echo ""
echo -n " Please press RRTURN to continue -> : "
set blank = $<
clear
else if ( $choice == 2 ) then
clear
echo ""
echo ""
echo ""
echo ""
echo ""
echo ""
echo ""
echo ""
echo ""
echo ""
echo ""
echo "
echo " USAGE OF THE PROGRAM "
echo " ~~~~~ "
echo " | "
echo " | "
echo " | 1. Run 'iraqautosong' program one hour after IT | "
echo " | injection of HFB. | "
echo " | "
echo " | 2. Move the data with the longest delay to this | "
echo " | program's directory. | "
echo " | "
echo " | 3. Rename the data as 'clearance_raw.1' or any name | "
echo " | you prefer, but it must end with extension '.1'. | "
echo " | "
echo " | 4. Rerun 'iraqautosong' every 30 min or any reasonable | "
echo " | time interval you prefer. | "
echo " | "
echo " | 5. Repeat steps 2, 3, and 4. But renamed data must | "
echo " | end with '.2', '.3', '.4', etc. | "
echo " | until 11 data sets have been acquired and properly | "
echo " | renamed. | "
echo " | "
echo " | 6. Run this program and follow the instructions on | "
echo " | the screen. | "
echo " | "
echo " | "
echo " ~~~~~ "
echo ""
echo ""
echo ""
echo ""
echo ""

```



```
echo "      Bye, Bye  !    "  
echo ""  
echo ""  
endif
```

```
# end of while  
end
```

```
unset blank  
quit:
```

```

# Omega Sourceable Script
# Filename: clear_rate_sub1
# This is the first subroutine called by main program clear_rate
# Purpose: To display the T (clearance rate) fitting curve
#           and compute the clearance rate
# Author: Yulin Song
# Time: June 1998
# Status: OK
# Potential Problem: The model involed ln(x) function may not result in a
#                    convergent fitting.
#                    In this case, two models could be used:
#                    Y = SLOPE*x + INTERCEPT or
#                    Y = Y0*exp(-x/T)

```

```

set file_dir = "$home/yulindata"
set fn =
set n =
set time_interval =

```

```

set fn_temp =
set n_temp =
set time_interval_temp =
set loop = N

```

```

while ( ( $loop == N ) || ( $loop == n ) )

```

```

    clear

```

```

    echo ""

```

```

    echo ""

```

```

    echo ""

```

```

    echo ""

```

```

    echo ""

```

```

    echo ""

```

```

    echo ""

```

```

    echo ""

```

```

    echo ""

```

```

    echo ""

```

```

                                T FITTING CURVE PARAMETER MENU

```

```

    echo ""

```

```

    echo ""

```

```

    echo ""

```

```

    echo ""

```

```

    echo "

```

```

        1. PROGRAM NAME:           = Clearance_rate

```

```

    echo ""

```

```

    echo "

```

```

        2. CURRENT DIRECTORY:      = $file_dir

```

```

    echo ""

```

```

    echo "

```

```

        3. FILENAME BASE:          = $fn

```

```

    echo ""

```

```

    echo "

```

```

        4. NUMBER OF FILES:        = $n

```

```

    echo ""

```

```

    echo "

```

```

        5. TIME INTERVAL FILE     = $time_interval

```

```

    echo ""

```

```

    echo ""

```

```

    echo ""

```

```

    echo ""

```

```

    echo ""

```

```

echo ""
echo ""
echo ""
echo ""
echo ""
echo ""
echo ""
echo ""
echo ""
echo ""
echo ""
echo ""
echo ""
echo ""
echo ""
echo -n "      Please enter FILENAME BASE -> "
set fn = $<
if ( $fn != "" ) then
    set fn_temp = $fn
else
    set fn = $fn_temp
endif
clear
echo ""
echo ""
echo ""
echo ""
echo ""
echo ""
echo ""
echo ""
echo ""
echo ""
echo ""
echo ""
echo "
                                T FITTING CURVE PARAMETER MENU                                "
echo ""
echo "
~~~~~"
echo ""
echo "          1. PROGRAM NAME:          = Clearance_rate          "
echo ""
echo "          2. CURRENT DIRECTORY:     = $file_dir              "
echo ""
echo "          3. FILENAME BASE:         = $fn                    "
echo ""
echo "          4. NUMBER OF FILES:       = $n                     "
echo ""
echo "          5. TIME INTERVAL FILE     = $time_interval         "
echo ""
echo "
~~~~~"
echo ""
echo ""
echo ""
echo ""
echo ""
echo ""
echo ""
echo ""

```

```

echo ""
echo ""
echo ""
echo ""
echo ""
echo ""
echo ""
echo ""
echo -n "      Please enter the NUMBER OF FILES -> "
set n = $<
if ( $n != "" ) then
    set n_temp = $n
else
    set n = $n_temp
endif
clear
echo ""
echo ""
echo ""
echo ""
echo ""
echo ""
echo ""
echo ""
echo ""
echo "
                                T FITTING CURVE PARAMETER MENU                                "
echo ""
echo ""
echo "      ~~~~~~"
echo "
1. PROGRAM NAME:      = Clearance_rate      "
echo ""
echo "      2. CURRENT DIRECTORY:  = $file_dir      "
echo ""
echo "      3. FILENAME BASE:      = $fn      "
echo ""
echo "      4. NUMBER OF FILES:      = $n      "
echo ""
echo "      5. TIME INTERVAL FILE  = $time_interval      "
echo ""
echo "      ~~~~~~"
echo ""
echo ""
echo ""
echo ""
echo ""
echo ""
echo ""
echo ""
echo ""
echo ""
echo ""
echo ""
echo ""

```

```

echo ""
echo ""
echo ""
echo ""
echo -n "      Please enter the TIME INTERVAL FILE -> "
set time_interval = $<
if ( $time_interval != "" ) then
    set time_interval_temp = $time_interval
else
    set time_interval = $time_interval_temp
endif
clear
echo ""
echo ""
echo ""
echo ""
echo ""
echo ""
echo ""
echo ""
echo ""
echo ""
echo ""
echo "
                                T FITTING CURVE PARAMETER MENU                                "
echo ""
echo "      ~~~~~~"
echo ""
echo "          1. PROGRAM NAME:          =  Clearance_rate          "
echo ""
echo "          2. CURRENT DIRECTORY:     =  $file_dir              "
echo ""
echo "          3. FILENAME BASE:         =  $fn                    "
echo ""
echo "          4. NUMBER OF FILES:       =  $n                      "
echo ""
echo "          5. TIME INTERVAL FILE     =  $time_interval         "
echo ""
echo "      ~~~~~~"
echo ""
echo ""
echo ""
echo ""
echo ""
echo ""
echo ""
echo ""
echo ""
echo ""
echo ""
echo ""
echo ""
echo ""
echo ""
echo ""
echo ""
echo ""
echo ""

```



```

echo -n "Are the entries correct (Y for correct and N for wrong) -> : "
set loop = $<
end
# end of while

stackrm *
get $fn.1
dis
@ fit_another_voxel = 1
while ( $fit_another_voxel )
# the first while statement
echo ""
echo "    Please enter the coordinates of the voxel to be plotted: "
echo ""
echo -n "    X = -> "
set col = $<
cal -o col $col 1 sub      # col = col - 1
echo ""
echo -n "    Y = -> "
set row = $<
echo ""

stackrm *
rm -f %tmp

@ ex = $n
while ( $ex >= 1 )
# get the files in descenting order i.e. in decreasing signal
# intensity order
    get $fn.$ex
    @ ex--
end

# cp $fn.1 junk
# get junk
header -i d0 dim0      # no of columns: acquisition direction
header -i d1 dim1      # no of rows: phase encoding direction
header -i d2 dim2
header -i tau ti
header -i naq na      # no of acquisitions
# header -i time_interval date # debug read in the time when the data
# was acquired

# echo " time_interval = $time_interval" # debug

# echo "d0 = $d0"      # debug
# echo "d1 = $d1"      # debug
# echo "d2 = $d2"      # debug
# get -a              # debug
# echo "tau = $tau"    # debug
# echo "naq = $naq"    # debug

```

```

rm -f t1_$fn
rm -f rawimdata
rm -f rawimheader
rm -f $fn.errmap

# view 1 1 $row          # view the rowth data set along acquisition
                        # direction. one row at a time
# printdata -r $col 1 > %tmp    # print data (real and imag) into file
                        # %tmp

# printdata -r $col 1      # debug

# shellset amp = %tmp      # assign the data point (real and imag)
                        # to 1D array amp
                        # the index of the array begins from 1 and
                        # amp[0] contains a space character
                        # amp[1] contains the real part and amp[2]
                        # contains the imaginary part of the data

# Normalize the signal intensity for multiple acquisitions to
# keep correct magnitude
# cal -o int $amp[1] $naq div          # int = amp[1]/naq
# echo " amp[1] = $amp[1] int = $int " # debug
# cal -o int $int 100 mul

# Obtain the amplitude at the logest delay as the initial estimate of A
header -i naq na
view 1 1 $row          # view the rowth block FFT transformed data set
                        # along acquisition direction
printdata -r $col 1 >temp
shellset A_initial = temp
cal -o A_initial $A_initial[1] $naq div
rm -f temp
cal -o A_initial1 $A_initial[1] lne

cal -o m $n 1 sub      # m = n - 1
# echo " n = $n "      # debug
# header -i tau ti
# cal -o tau $tau 1000000 div    # tau = tau / 1000000
# view 1 1 $row          # view the data with the longest delay,
                        # which is on the top of the stack
# printdata -r $col 1 > amp_longest_tmp # at the moment. Then read
                        # the data into

amp_longest_tmp
# shellset amp_longest = amp_longest_tmp # amp_longest_tmp is a file
# rm -f amp_longest_tmp

```

```

# Write the text and data into input file: clear_rate_lsq_in
rm clear_rate_lsq_in
@ col_tmp = $col + 1
cat $time_interval >! time_temp          # read the time interval and
                                           # store in array time_inter_temp
shellset time_inter_temp = time_temp     # new code

# echo "    col_tmp = $col_tmp " # debug
echo "Lsqfit Input Data" >>clear_rate_lsq_in
echo "File Base: $fn    Voxel: ( X = $col_tmp, Y = $row )"
>>clear_rate_lsq_in
echo "Fit to Clearance Model: ln(Q(x)) = ln(Q0)- x/T " >>clear_rate_lsq_in
echo "ClearanceModel 2 ln(Q0)-x/T " >>clear_rate_lsq_in
echo "Q0 $A_initial1 1 1/Q0 " >>clear_rate_lsq_in
echo "T 700 1 x/(T*T) " >>clear_rate_lsq_in
echo "Time(mins) ln(Signal_Intensity) " >>clear_rate_lsq_in
echo " $time_inter_temp[1] $A_initial1 " >>clear_rate_lsq_in

    @ ex1 = 1
    while($ex1 <= $m)
    # EXCHANGE POSITIONS OF FILE $EX1 TO ZERO (TOP) OF STACK
    @ index = $ex1 + 1
    stackmv $ex1 0
# get -a # debug
# READ PIXEL MAGNITUDE INTO SHELL VARIABLE
# get -a # debug
view 1 1 $row
printdata -r $col 1 > %tmp
shellset ampl = %tmp
rm -f %tmp

# READ HEADER VARIABLES FOR T FIT
# header -i tau ti # tau = ti
# header -i naq na # naq = na
cal -o ampl[1] $ampl[1] $naq div # ampl[1] = ampl[1]/naq
cal -o ampl $ampl[1] lne # ampl = ln(ampl[1])
# cal -o tau $tau 1000000 div # tau = tau/1000000
# echo "tau = $tau Amplitude = $ampl[1]" # debug

# @ time_scale = $time_interval + $time_scale
echo " $time_inter_temp[$index] $ampl " >>clear_rate_lsq_in
stackmv 0 $ex1
@ ex1++
end
# ENDWHILE

cat clear_rate_lsq_in
echo ""
lsqtool clear_rate_lsq_in
echo -n " Do you want to fit another voxel (y/n) ? -> "
set fit_again = $<
echo ""

```

```

if ( $fit_again != y && $fit_again != Y ) then
    echo ""
    echo "      Bye Bye ! "
    echo ""
    exit(4)
else
    @ time_scale = 0
    @ fit_another_voxel =1
endif

end
# end of first while
unset n ex1 ex fit_another_voxel col_tmp time_interval

```



DEPARTMENT OF THE ARMY  
US ARMY MEDICAL RESEARCH AND MATERIEL COMMAND  
504 SCOTT STREET  
FORT DETRICK, MARYLAND 21702-5011

REPLY TO  
ATTENTION OF:

MCMR-RMI-S (70-1y)

26 Nov 02

MEMORANDUM FOR Administrator, Defense Technical Information  
Center (DTIC-OCA), 8725 John J. Kingman Road, Fort Belvoir,  
VA 22060-6218

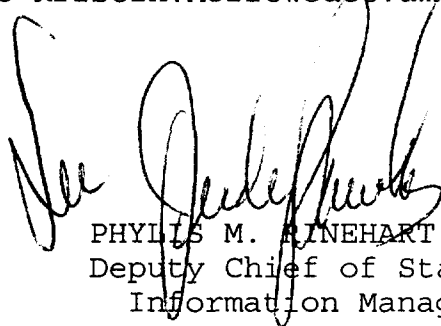
SUBJECT: Request Change in Distribution Statement

1. The U.S. Army Medical Research and Materiel Command has reexamined the need for the limitation assigned to technical reports written for this Command. Request the limited distribution statement for the enclosed accession numbers be changed to "Approved for public release; distribution unlimited." These reports should be released to the National Technical Information Service.

2. Point of contact for this request is Ms. Kristin Morrow at DSN 343-7327 or by e-mail at Kristin.Morrow@det.amedd.army.mil.

FOR THE COMMANDER:

Encl



PHYLLIS M. PINEHART  
Deputy Chief of Staff for  
Information Management

ADB263708  
ADB257291  
ADB262612  
ADB266082  
ADB282187  
ADB263424  
ADB267958  
ADB282194  
ADB261109  
ADB274630  
ADB244697  
ADB282244  
ADB265964  
ADB248605  
ADB278762  
ADB264450  
ADB279621  
ADB261475  
ADB279568  
ADB262568  
ADB266387  
ADB279633  
ADB266646  
ADB258871  
ADB266038  
ADB258945  
ADB278624